Enhanced Feedback between Shallow Convection and Low-level Moisture Convergence Leads to Improved Simulation of MJO Eastward Propagation

Yan Liu, Zhe-Min Tan*

School of Atmospheric Sciences and Key Laboratory of Mesoscale Severe Weather/MOE, Nanjing University, Nanjing, China

Zhaohua Wu

Department of Earth, Ocean and Atmospheric Science, and Center for Ocean-Atmospheric Prediction Studies, Florida State University, Tallahassee, Florida

*Corresponding author: Zhe-Min Tan. School of Atmospheric Sciences, Nanjing University, Nanjing, 163 Xianlin Avenue, Nanjing 210023, China.

E-mail: zmtan@nju.edu.cn.

Abstract

Recent study indicates that the noninstantaneous interaction of convection and circulation is essential for large-scale convective systems. It is incorporated into cumulus parameterization (CP) by relating cloud-base mass flux of shallow convection to a composite of subcloud moisture convergence in the past. Three pairs of 19-yr simulations with original and modified CP schemes are conducted in a tropical channel model to verify their ability to reproduce the MJO. Improved eastward propagation signal and stronger intraseasonal variability are observed in the simulations with the modified CP schemes based on the noninstantaneous interaction. It is found that enhanced feedback between shallow convection and low-level moisture convergence results in amplified shallow convective heating and/or extended heating duration, shaping tilted heating as in observations. It also generates enhanced moisture convergence which transports more moisture upward. The improved simulations of eastward propagation of the MJO are largely attributed to higher specific humidity in the lower troposphere to the east of maximum rainfall center, which is related to stronger boundary layer moisture convergence forced by shallow convection. Large-scale horizontal advection causes asymmetric moisture tendencies relative to rainfall center (positive to the east and negative to the west) and also gives rise to eastward propagation. The zonal advection, especially the advection of anomalous specific humidity by mean zonal wind, is found to dominant the difference of horizontal advection between each pair of simulations.

1. Introduction

The Madden-Julian oscillation (MJO) is a planetary-scale convectively coupled equatorial wave that usually propagates eastward at a speed of 5-8 m s^{-1} (see Zhang (2005) for a complete review). The MJO has long been the focus of research community for its far-reaching influences on global climate and weather systems (Lau and Waliser 2012; Zhang 2013). Though much improvement in the simulations of MJO has been made in terms of model resolution, physical parameterization, air-sea coupling, etc., general circulation models still struggle to realistically simulate the MJO (Lin et al. 2006; Hung et al. 2013; Jiang et al. 2015). Among the most salient features that should be reproduced, eastward propagation is hardly captured by models participating in the MJO task force global model comparison project (Jiang et al. 2015). More than two thirds of participating models show a stationary or even westward propagating intraseasonal signals.

Associated with the eastward-moving convective envelope of the MJO, a prominent transition from convectively suppressed to active phase can be observed in the regions of equatorial Indian and western Pacific oceans (Hendon and Salby 1994; Johnson and Ciesielski 2013). During the transition period, clouds over the region also develop gradually from shallow cumulus/congestus mode to deep convective and stratiform mode (Kikuchi and Takayabu 2004; Riley et al. 2011; Xu and Rutledge 2016). Considering the significant importance of tropospheric moisture content for tropical convection (Bretherton et al. 2004; Holloway and Neelin 2009, Ahmed and Schumacher 2018), it is proposed that shallow convection serves to moisten the lower troposphere for subsequent transition to deep convection and thus is vital for the eastward propagation of the MJO.

A direct moistening mechanism related to shallow convection is vertical transport of the tropospheric moisture. Benedict and Randall (2007) conducted moisture-budget analysis using reanalysis data and found that vertical advection by shallow cumulus dominated moisture tendency prior to the onset of deep convection. This gradual increase of positive moisture and temperature anomaly corresponds to the “recharge” process of organized convection in the tropics (Bladé and Hartmann 1993; Kemball-Cook and Weare 2001). By comparing performance of parameterized shallow and deep cumulus in the global compressible nonhydrostatic Model for Prediction Across Scales (MPAS), Pilon et al. (2016) showed that shallow convection plays a key role in transporting moisture upward to the lower and middle troposphere and then enhances diabatic heating and precipitation. Many other studies also come to a similar conclusion though different observation data or numerical simulations are analyzed (e.g., Hagos and Leung 2011; Del Genio et al. 2012; Bellenger et al. 2015; Janiga and Zhang 2016; Hirota et al. 2018).

However, local (convective scale) moistening of shallow cumulus and congestus clouds seems inadequate to explain the observed increase in lower-troposphere moisture. According to the estimation made by Hohenegger and Stevens (2013) with bulk analysis and large-eddy simulations, actual time taken by the transition from congestus to deep convection is much shorter than that needed for congestus clouds to sufficiently moisten the atmosphere. They suggested that upward motion forced by large-scale disturbances may contribute to the extra moistening. Hagos et al. (2014) conducted a regional cloud-resolving simulation that captures the shallow-to-deep convection transition of the MJO. Their results indicate that the probability of transition is highly sensitive to midlevel large-scale humidity and uplift. The increased moisture at midlevel can also be attribute to large-scale updraft. Observation analysis with satellite (Masunaga 2013) and radar (Kumar et al. 2013) data both confirm the significant moistening by large-scale process. Particularly, Masunaga (2013) highlighted the importance of large-scale upward transport of moisture and heat through cloud base (i.e., large-scale convergence in subcloud layer) to this moistening, especially in organized convective systems.

Evidence also exists that interaction between large-scale disturbances and shallow convective heating/moistening favors initiation and propagation of MJO convection (e.g., Hsu and Li 2012; Ruppert and Johnson 2015; Rowe and Houze 2015). Wave-CISK is one of the mechanisms that explain the interaction, but horizontal scale predicted by wave-CISK is unrealistically small (Crum and Dunkerton 1992; Matthews and Lander 1999). Recently, Liu et al. (2019, hereafter LTW19) revealed that bottom-heavy heating profile of shallow convection drives intense wind response and converges low-level moisture, which effectively feeds back to diabatic heating via upward transport and condensation. This cooperative interaction between shallow convection and low-level moisture convergence may lead to unstable growth and upscale organization of convection systems. Unlike conventional wave-CISK, feedback in LTW19 is noninstantaneous as the time is needed for convective heating to force low-level moisture convergence, and moisture convergence to moisten and heat the lower troposphere as well. Although the noninstantaneous wave-CISK mechanism has been proved to be able to capture the eastward propagation of large-scale Kelvin wave signals quite well in an idealized model as in LTW19, its performance in reproducing the propagation of the MJO in a more realistic model configuration still needs to be verified.

A tropical channel configuration of the Weather Research and Forecasting (WRF; Skamarock et al. 2008) model is widely used to test mechanisms of the MJO (Ray et al. 2011; Ulate et al. 2015; Hall et al. 2017), for its convenience in choosing different boundary conditions and physical parameterizations. In the present study the tropical channel model is used with cumulus parameterizations (CPs) modified to incorporate the basic idea of noninstantaneous convection-circulation interaction based on the theorical diagram in LTW19. Comparison is made between simulations with original and modified CP schemes to see how feedback between shallow convection and low-level moisture convergence (hereafter FSM) influence convective organization and promote eastward propagation of the MJO. Relative contributions of convergence (vertical transport) and horizontal advection are identified.

The remainder of the paper is arranged as follows. We first briefly introduce the basic concept of noninstantaneous wave-CISK in section 2. In section 3, introduction of data sources, model settings and modification of CP scheme is given. Section 4 presents mean-state features of simulations with different CP schemes. Section 5 and 6 compare related processes that lead to enhanced FSM and improved eastward propagation. Discussion and summary are offered in section 7 and 8.

2. Noninstantaneous wave-CISK

It is compelling that the time scale of large-scale system is larger than that of individual cumulus convection embedded in it. As small-scale convective process can be regarded as instantaneous (ignoring the convective time scale of hours), large-scale system is rather noninstantaneous. The time scale generally comes from two main aspects of large-scale convective process (or two legs of convection-circulation feedback). Firstly, even suitable dynamical condition for convection is provided by large-scale circulation, it still takes time for numerous clouds to moisten the troposphere through detrainment and re-evaporation of precipitation and thus morphological structures could be built up (Johnson and Ciesielski 2013; Powell and Houze 2015). Secondly, time is also needed for the forced response to convective heating to propagate out and serve the development and propagation of convective system (e.g., Wu 2000).

In order to represent this noninstantaneous character of the FSM, LTW19 constructed a simple cumulus parameterization scheme in which shallow convective heating is determined by the weighted mean of subcloud moisture convergence in the past period, i.e.,

$$M^{*} = \int_{t-\tau}^{t} rM dt_i \bigg/ \int_{t-\tau}^{t} r dt_i \,, \tag{1}$$

where M is the subcloud moisture convergence at the time of t_i, t is the current time, τ is the specific time scale of composite, which is called the accumulation-consumption time scale of moisture in LTW19. The quantity r is a time dependent weighting function of which the definition is:

$$r = 1 - [\frac{t_i - (t - \tau/2)}{\tau/2}]^2, \qquad t - \tau \le t_i \le t. \tag{2}$$

In this circumstance, moisture convergence keeps nourishing convective development (by releasing latent heat) for a period of τ once it is forced by convective heating. On the other hand, convective heating is also slowly varying and exerting long-term influence on the atmosphere.

3. Data and model runs

3.1. Data

The European Center for Medium-Range Weather Forecasting (ECMWF) ERA-Interim reanalysis data (Dee et al. 2011) are used for model initiation and lateral boundary conditions. Atmospheric state computed with ERA-interim data is also referred to as observation. Sea surface temperature (SST) data is obtained from NOAA 1/4° daily Optimum Interpolation Sea Surface Temperature Analysis Version 2 (OISSTv2; Reynolds et al. 2007). In order to validate simulated rainfall and propagation signal of MJO, we utilize data of the Global Precipitation Climatology Project (GPCP) daily precipitation estimates (Huffman et al. 2001) and the National Oceanic and Atmospheric Administration (NOAA) Climate Data Record (CDR) of Daily Outgoing Longwave Radiation (OLR; Lee and NOAA CDR Program 2011). Both of them are daily analysis data defined on a global 1.0° × 1.0° longitude-latitude grid.

3.2. Model configuration

The model used is the WRF Model version 3.7.1 with a tropical channel configuration, which is similar to that of Ray et al. (2009) and Hall et al. (2017). Horizontal resolution is set to 1.0° × 1.0°. 32 model levels are placed vertically with the top level at 50 hPa. The model domain is periodic in the zonal direction and bounded at 30°S and 30°N in the meridional direction. Geopotential, temperature, relative humidity, and zonal and meridional winds from ERA-Interim reanalysis are interpolated to model grids at these boundaries. Prescribed SST from OISSTv2 interpolated to 1° resolution and 4 times daily is also used as lower boundary to force the model. The followings are the physical parameterization schemes used in this study: the WRF single-moment 3-class simple ice scheme (Hong et al. 2004), the Yonsei University planetary boundary layer scheme (Hong et al. 2006) with a surface layer scheme based on the Monin-Obukhov similarity theory (Monin and Obukhov 1954), the unified NOAA land-surface model (Chen and Dudhia 2001), the Rapid Radiative Transfer Model for longwave scheme (Mlawer et al. 1997), and the Dudhia (1989) shortwave scheme.

FSM emphasizes the importance of low-level moisture convergence forced by shallow convection to upward transport of moisture and heat, which is usually determined by mass flux at cloud base in some CPs. To facilitate modification and analysis, three mass-flux type CP schemes with particular treatments of shallow convection are chosen for the control runs in the present study. These schemes are the new Simplified Arakawa-Schubert (SAS) scheme (Han and Pan, 2011), the new Tiedtke (TDK) scheme (Zhang and Wang, 2017), and the Kain-Fritsch scheme (Kain, 2004) with the Ma-Tan trigger (Ma and Tan, 2009; hereafter KFMT). The new trigger is used in Kain-Fritsch scheme for its better performance under weak synoptic forcing. Although these schemes differ greatly in their treatment of convective process (see the listed papers above and the references therein), they can all be divided into relatively separated parts, i.e., convective trigger, cloud model and closure assumption. Here we modify closure assumptions of these three schemes to that constructed based on the noninstantaneous wave-CISK.

3.3. Modification of cumulus parameterization

According to LTW19, two main facts that should be considered in CP are: 1) shallow convection drives low-level moisture convergence which is strong enough to sustain itself, while deep convection does not; 2) feedback between shallow convection and low-level moisture convergence is noninstantaneous and usually takes a couple of days for large-scale convection systems. Noninstantaneous wave-CISK assumes that convective heating rate is proportional to low-level moisture convergence, but in mass-flux type CP schemes, it is difficult to assign heating rate directly. Closure assumptions of SAS, TDK and KFMT all relate cloud-base mass flux to boundary layer process (Table 1), which controls the intensity of shallow convective activity. As noted by Arakawa (2004), boundary layer moisture convergence is the dominant contributor to moisture flux tendency. Suhas and Zhang (2015) also confirmed the significant positive correlation between moisture convergence and mass flux. Here cloud-base mass flux is set to be proportional to a composite of subcloud moisture convergence in the past. In this way, shallow convective heating is related to low-level moisture convergence indirectly. We still use Eq. (1) and (2) to calculate the composite of moisture convergence. The time scale τ, which can be regarded as the time needed for moisture convergence to force upward mass flux, is set to 6 h after several sensitive tests. Low-level moisture convergence is calculated as:

$$\begin{aligned} M &= -\int_0^{z_b} \rho \nabla_h \bullet (\mathbf{v}q) dz \\ &= -\int_0^{z_b} \rho q \nabla_h \bullet \mathbf{v} dz - \int_0^{z_b} \rho \mathbf{v} \bullet \nabla_h q dz, \end{aligned} \tag{3}$$

where ρ and q are the density of air and the specific humidity respectively, z_b is the height of cloud base (calculated in each CP schemes), and $\mathbf{v}$ is horizontal velocity. The last two terms in Eq. (3) represent mass convergence and horizontal moisture advection respectively. The modified closure assumption can thus be written as:

$$F = \begin{cases} \alpha M^*, & M^* > 0 \\ 0, & M^* \leq 0, \end{cases} \tag{4}$$

where F is cloud-base mass flux, α is a factor tuned in each CP schemes. Except for closure assumption of shallow convection parameterization, other aspects of CP are kept unchanged.

The procedure to distinguish deep and shallow convection follows that of original CP schemes. Table 1 summaries the criteria for shallow convection in each scheme. At each time step, subcloud moisture convergence (M) is saved once the criteria for shallow convection are satisfied, but shallow convection will not be activated until the time composite of moisture convergence (M^*) turns positive. After the transition from shallow to deep convection, stored memory of moisture convergence is eliminated for the consumption of them by deep convection is very fast (LTW19). It should also be noted that definitions of shallow convection are different in these schemes, but the main conclusion drawn in this study is not altered by the difference.

4. Mean-state feature

In this study, six 19-yr simulations from 1996 to 2014 are carried out with original (denoted as SAS, TDK and KFMT, respectively) and modified (denoted as SAS-n, TDK-n and KFMT-n, respectively) CP schemes. Diagnostics are focused on boreal winters (November-April) during this period. Averaged winter precipitation for observation and simulations is shown in Fig. 1. All the experiments with original CP schemes reproduce rain belts along climatological convergence zones in the western Pacific and over the Maritime Continent, though the amount of rainfall is generally overestimated (left panels of Fig. 1). However, these simulations miss the rainfall center in the eastern Indian Ocean and produce too much rainfall in the middle to western Indian Ocean. In the right panels, boreal winter-mean precipitation differences between modified and original schemes are displayed. Although the modification is only made to shallow convection which basically is nonprecipitating, rainfall is still modulated through interaction between shallow and deep convection. The modulation is quite moderate over the simulation region, except that precipitation is largely suppressed over the Maritime Continent in TDK-n. It means deep convection is largely mitigated in this case.

As rainfall is overestimated in the Indian Ocean, so is the MJO-filtered precipitation variance (Fig. 2). Here only eastward-propagating signals with zonal wavenumbers 1–5 and periods 20–100 days are saved in order to filter MJO-related precipitation. Modification of shallow convection schemes is able to raise the precipitation variance to a level close to observation, but the location is still uncorrected. The precipitation variance over the Maritime Continent in TDK-n also decreases as precipitation itself.

In the following analyses, a lag-regression/correlation method is used. Before calculating regression/correlation coefficient, the climatological annual cycle (annual mean and three leading harmonics) is removed first, and then a 20–100 day band-pass filtering is operated with Butterworth filter. Regression/correlation coefficients are thus calculated against anomalies averaged over a box (80–90°E; 5°S–5°N) in the Indian Ocean. Lag correlations of filtered OLR with itself averaged over the box is shown in Fig. 3. Compared to observations, the propagation signals in control runs are rather weak and confined in the Indian Ocean area. Modification of shallow convection schemes helps to strengthen the eastward propagation of convection systems and extend them further into the western Pacific Ocean. Notice that the most significant improvement is observed in TDK-n (Fig. 3e), but the rainfall and its variance are decreased markedly (Figs. 1e and 2e). It suggests that vigorousness of shallow convection may lead to a suppression of deep convection.

Following Wheeler and Kiladis (1999), the wave number-frequency power spectra of equatorially symmetric component of tropical OLR between 15°S and 15°N is depicted in Fig. 4. Although control runs are able to reproduce the spectral power peak in the right range corresponding to MJO, its amplitude is reduced to a much lower level.

The modification of CPs generally augments the spectral power, especially in TDK-n and KFMT-n.

5. Enhanced feedback between shallow convection and low-level moisture convergence

As seen from above assessments, modification of shallow convection produces stronger intraseasonal variability and more importantly the improved eastward propagation. To figure out how the noninstantaneous moisture convergence closure improve MJO simulations, we will investigate the process of FSM first. Moisture content has been recognized to dominate the buildup and propagation of MJO convection (Sobel and Maloney 2012; Raymond and Fuchs 2009; Majda and Stechmann 2009). Fig. 5 displays lagged regression of specific humidity anomaly at 850 hPa against rainfall over the Indian Ocean, together with regressed zonal wind at the same level. With the implication of new shallow convection closure, moisture and zonal wind anomalies increase, propagation signals extend to the further east, and the propagation speed slows down to that of the MJO (8 m s^{-1}). According to Wu (2003), decreased propagation speed is due to the smaller equivalent depth corresponding to enhanced shallow convection. Another noteworthy feature is that moisture anomalies lag easterly winds and collocate with the convergence zone of easterly winds. Above analysis indicates a concurrent enhancement of large-scale convergence, shallow convection, and low-level moisture content.

To display the changes of FSM brought about by noninstantaneous moisture convergence closure, we calculate lag-regression of 10°S-10°N averaged diabatic heating at the longitude of 90°E against intraseasonal precipitation over the Indian Ocean. The total diabatic heating is derived with a residual budget analysis based on the temperature equation (Yanai et al., 1973; Ling and Zhang, 2011). Vertical-time regression pattern is shown in Fig. 6. The vertical backward tilting of diabatic heating is clearly seen in observation, but few of the control runs reproduce this tilted structure. As modified closure strengthens shallow convective heating which usually leads the main convective heating of MJO, simulations with modified CP schemes show more tilted heating structures. In simulations with TDK scheme, the time lag between shallow and deep convection on intraseasonal timescales is so short that they burst almost at the same time (Fig. 6d). Modification of shallow convection closure marginally alters the time lag, but it effectively enhances shallow convective heating and inhibits deep convective heating (Fig. 6e).

As in Fig. 6, the regression patterns of mass convergence and horizontal moisture advection terms composing moisture convergence (rhs terms of Eq. 3) are plotted in Figs. 7 and 8, respectively. The magnitude of horizontal advection is about one order smaller than that of mass convergence, so it is the mass convergence term that dominates moisture convergence. Similar to that of diabatic heating, regression patterns of mass convergence also show tilted structures which are better captured with modified CP schemes. Since shallow convection transports moisture upward (Benedict and Randall 2007; Pilon et al. 2016), enhanced shallow convection helps to extend mass convergence zone to higher levels. In contrast, horizontal advection of moisture usually leads diabatic heating by about 10 days. Larger positive moisture advection seen near day -10 in modified simulations may be related to more suppressed convection ahead of major convection (Kim et al., 2014). This positive moisture advection contributes to moisture convergence and thus helps to trigger noninstantaneous convection-circulation feedback. Afterwards, enhanced shallow convection induces stronger moisture advection in the boundary layer (near day 0 in Fig. 8). It also helps to transports more moisture to higher levels and increase moisture content in the lower troposphere.

To better illustrate the influence of shallow convection closure on FSM, evolutions of regressed diabatic heating in the lower troposphere (850 hPa) and moisture convergence in the boundary layer (925 hPa) are plotted in Fig. 9. These two particular layers are chosen because shallow convective heating usually peaks at 850 hPa and moisture convergence maximizes and is vertically uniform in the boundary layer (Fig. 7). In observation, diabatic heating leads boundary layer moisture convergence, which may be related to the fact that anomalous short wave heating starts near the surface before day -10 when convection is suppressed (Ciesielski et al. 2017). Numerical simulations seem not able to reproduce this time lag. Low-level diabatic heating and moisture convergence are almost in phase therein. Introducing a shallow convection closure based on the noninstantaneous wave-CISK helps to extend heating duration (Fig. 9b), increase heating amplitude (Fig. 9c), or both (Fig. 9d), and strengthen boundary layer moisture convergence as well. Although LTW19 suggests noninstantaneous convection-circulation feedback should be able to alter the phase relationship between heating and moisture convergence, a finer time resolution is needed to display this change.

6. Eastward propagation of MJO convection

The remained question is, how this enhanced FSM promotes eastward propagation of MJO convection. Fig. 10 displays horizontal patterns of regressed moisture convergence at 925 hPa and horizontal winds at 850 hPa. Note that convection (precipitation) center is located in the Indian Ocean box (80°-90°E; 5°S-5°N). The prominent feature of observation is that boundary layer moisture convergence extends to the east of MJO convection center and all the way to the western Pacific Ocean. Easterly winds are prevalent over the Indo-Pacific warm pool region and located to the further east of moisture convergence. These features can also be found in numerical simulations, with increased convergence and easterly winds over the warm pool region in SAS-n and KFMT-n. In the simulations with TDK type schemes, eastward extension of low-level moisture convergence is narrowly confined near the convection center over the Indian Ocean, which is consistent with the little vertical tilt in regressed heating structure (Fig. 6). Besides the enhanced shallow convective heating, boundary layer friction may also contribute to the increased moisture convergence (Wang and Rui 1990; Hsu and Li 2012).

Vertical-longitude regressions of specific humidity anomaly averaged between 10°S and 10°N associated with rainfall over the Indian Ocean box are shown in Fig. 11. Westward tilt of specific humidity can be observed in observation, with positive moisture anomaly in the lower troposphere to the east of convection center (80°-90°E). Comparing simulation results with different CP schemes, the biggest change is the enhanced positive moisture anomaly in lower levels to the east of 90°E, corresponding to the enhanced moisture convergence zone (Fig. 10).

Following Eq. 3, moisture convergence is decomposed into two terms associated with mass convergence and moisture advection. Difference between regressed moisture convergence terms at 925 hPa are plotted in Fig. 12. Obviously, mass convergence term dominates moisture convergence. In SAS simulations, modified CP scheme increases moisture convergence along the equator from the middle Indian Ocean to the western Pacific Ocean. While in the other two cases moisture convergence increments are found in smaller regions, they help to foster new convection to the east of convection center all the same. In contrast, positive horizontal advection in the boundary layer is usually located in regions where vigorous deep convection present, which can also be deduced from Fig. 8.

Although advection term makes little contribution to the total amount of moisture convergence, it may noticeably modulate the propagation of MJO due to its asymmetric pattern relative to convection center. Here the longitude-height plot of horizontal moisture advection averaged in tropical belt (10°S–10°N) and the difference between simulations with modified schemes and original ones are shown in Fig. 13. In agreement with previous studies (Kim et al. 2014; Adames and Wallace 2015; Zhu and Hendon 2015), the asymmetric structure of horizontal advection relative to rainfall center also contributes to eastward propagation (Figs. 13a, 13b, 13d and 13f). It moistens the lower troposphere before the maximum rainfall (east of 90°E) while dries the lower troposphere after that (west of 90°E). Compared to control runs, modified schemes almost double the asymmetric advective tendencies and thus give rise to the eastward propagation (Figs. 13c, 13e and 13g).

Differences of horizontal moisture advection can be partitioned into contributions from zonal and meridional components. Fig. 14 displays differences of regressed zonal (Figs. 14a, 14c and 14e) and meridional (Figs. 14b, 14d and 14f) advection between simulations with modified CP schemes and control runs. Obviously, the difference of horizontal moisture advection mainly comes from the difference of zonal advection over the Indian and western Pacific Ocean. This result contradicts previous studies that the meridional component plays a key role in producing the asymmetric structure of horizontal moisture advection (Maloney 2009; Kim et al. 2014; Zhu and Hendon 2015). It may be related to enhanced shallow convection that usually locates to the east of maximum rainfall center and causes kelvin-wave response.

Following Maloney (2009) and Zhu and Hendon (2015), further analysis by separating horizontal advection into time mean and deviation from the time mean shows that the main contribution of the difference of regressed zonal advection is from that of advection of anomalous specific humidity by mean zonal wind (not shown). It means that, although enhanced shallow convection with modified CP schemes does not induce substantially stronger easterly winds to the east of 90°E (Fig. 10), it effectively moistens the lower troposphere there (Fig. 11), and then easterly winds advect anomalous moisture in the region of 90°E–120°E (see Fig. 14a, 14c and 14e).

7. Discussion

Previous studies demonstrate that shallow convection preconditions the atmosphere for the subsequent onset of active deep convection, which is fundamental to the eastward propagation of the MJO (Benedict and Randall 2007; Adames and Wallace 2015). However, if upward transport by large-scale forcing is not incorporated, shallow convection alone is not able to sufficiently moisten the lower troposphere (Hohenegger and Stevens 2013; Masunaga 2013; Kumar et al. 2013). In fact, shallow convective activity cannot be separated readily from its large-scale background, since a strong interaction exists between them. Notice that modified closure assumption of shallow convection only relates cloud-base mass flux to low-level moisture convergence. The feedback between shallow convection and low-level moisture convergence is not guaranteed therein. Improved simulation with modified CP scheme demonstrates that this feedback is an intrinsic character of large-scale convective system, and that the modified closure assumption helps to patch this feedback to make it work.

It is widely recognized that improved simulation of the MJO can be realized by increasing the sensitivity of deep convection to tropospheric humidity, such as increasing convective entrainment rate (Tokioka et al. 1988; Bechtold 2008; Benedict et al. 2014) or rain evaporation fraction (Maloney 2009; Hannah and Maloney 2011; Kim et al. 2012). These two modifications both help to suppress deep convection until other processes like shallow convection sufficiently moisten the atmosphere.

Noninstantaneous wave-CISK mechanism behaves quite similarly. Change of the ratio of shallow and deep convection in three pairs of simulations are plotted in Fig. 15. In agreement with above discussion, enhanced shallow convection is related to suppressed deep convection. KFMT scheme produces the largest increment of shallow convection, consistent with the strongest heating and moistening tendency seen in Figs. 6 and 11 in the lower troposphere. In this sense, merely modifying closure assumption seems inadequate to get a satisfying MJO simulation. Further work is required to study the interaction of shallow and deep convection and improve its description in CP scheme in the future.

Jiang et al. (2016) analyzed simulations with 25 climate models and observed an anti-correlation between convective time scale and MJO amplitude. The variable of convective time scale in their study is a measure of how rapidly precipitation must increase to remove excess column water vapor (see also Bretherton et al., 2004; Sobel and Maloney 2012). Similarly, the time scale (τ) here is a description of how rapidly converged moisture is transported upward through cloud base. $\tau = 6$ h used in modified CP schemes is a rather rough estimation. We cannot determine its exact value at this moment. Sensitivity tests show that increased time scale leads to decreased amplitude of intraseasonal variability and westward propagation tendency. Suhas and Zhang (2015) estimated a time lag between moisture convergence and mass flux of about 1 h using cloud-resolving model simulation. But their model domain is 256×256 km^2, which means only meso-scale or small-scale process is included. Considering the large-scale system we intend to deal with, the time scale of 6 h is a reasonable estimation. More study on the time scale τ with observations and high-resolution numerical simulations will be conducted in the future.

8. Summary

Based on the noninstantaneous wave-CISK proposed in LTW19, three CP schemes are modified to couple shallow convection with large-scale circulation through low-level moisture convergence in this study. Simulations with modified CP schemes show improved eastward propagation signals and stronger intraseasonal variabilities of convection (OLR) without degrading the mean states. Through positive feedback between shallow convection and large-scale circulation, the intrinsic instability of noninstantaneous wave-CISK incorporated in CP schemes results in amplified shallow convective heating and/or extended heating duration, shaping tilted heating structure as in observations (Fig. 6). On the other hand, enhanced moisture convergence transports more moisture upward with horizontal advection augmenting the moistening prior to deep convection onset (Fig. 7 and 8).

The eastward propagation of the MJO is highly sensitive to the lower troposphere moisture content. To the east of major convection center, strong boundary layer moisture convergence is forced by shallow convection, which effectively moistens the lower atmosphere. Large-scale horizontal advection gives rise to eastward propagation by causing positive moisture tendency in the front of convection center and negative tendency in the tail. Zonal component is found to dominant the changes of moisture advection brought about by modification of CP schemes. In addition, the difference of zonal advection mainly comes from the advection of anomalous specific humidity by mean zonal wind, which means FSM generates larger moisture anomaly than zonal wind anomaly.

Acknowledgements. This work is jointly supported by the National Key R&D Program of China under Grants 2017YFC1501601, the National Natural Science Foundation of China (61827901).The authors thank Pallav Ray for his suggestions on WRF model settings. We also thank Jianping Tang for providing ERA-Interim data, and Ming Bao for the help with data analysis.

References

Adames, Á.F. and J.M. Wallace, 2015: Three-dimensional structure and evolution of the moisture field in the MJO. *J. Atmos. Sci.*, **72**, 3733–3754.

Ahmed, F., and C. Schumacher, 2018: Spectral signatures of moisture–convection feedbacks over the Indian Ocean. J. Atmos. Sci., 75, 1995–2015.

Arakawa, A., 2004: The cumulus parameterization problem: Past, present, and future. *J. Climate*, 17, 2493–2525.

Bechtold, P., M. Kohler, T. Jung, F. Doblas-Reyes, M. Leutbecher, M. J. Rodwell, F. Vitart, and G. Balsamo, 2008: Advances in simulating atmospheric variability with the ECMWF model: From synoptic to decadal time-scales, *Quart. J. Roy. Meteor. Soc.*, **134**, 1337–1351.

Bellenger, H., K. Yoneyama, M. Katsumata, T. Nishizawa, K. Yasunaga, and R. Shirooka, 2015: Observation of moisture tendencies related to shallow convection. *J. Atmos. Sci.*, **72**, 641–659.

Benedict, J. J., and D. A. Randall, 2007: Observed characteristics of the MJO relative to maximum rainfall. *J. Atmos. Sci.*, **64**, 2332–2354.

——, E. D. Maloney, A. H. Sobel, and D. M. W. Frierson, 2014: Gross moist stability and MJO simulation skill in three full-physics GCMs, *J. Atmos. Sci.,* **71**, 3327–3349.

Bladé, I., and D. L. Hartmann, 1993: Tropical intraseasonal oscillation in a simple nonlinear model, *J. Atmos. Sci.*, **50**, 2922–2939.

Bretherton, C. S., M. E. Peters, and L. E. Back, 2004: Relationships between water vapor path and precipitation over the tropical oceans. *J. Climate*, 17, 1517–1528.

Chen, F., and J. Dudhia 2001: Coupling an advanced land‑surface/hydrology model with the Penn State/NCAR MM5 modeling system, Part I: Model description and implementation, *Mon. Wea. Rev.*, 129, 569–585.

Ciesielski, P. E., R. H. Johnson, X. Jiang, Y. Zhang, and S. Xie, 2017: Relationships between radiation, clouds, and convection during DYNAMO, *J. Geophys. Res. Atmos.*, 122, 2529–2548.

Crum, F. X., and T. J. Dunkerton, 1992: Analytic and numerical models of wave–CISK with conditional heating. *J. Atmos. Sci.*, 49, 1693–1708.

Dee, D. P., and Coauthors, 2011: The ERA-Interim reanalysis: Configuration and performance of the data assimilation system. *Quart. J. Roy. Meteor. Soc.*, 137, 553–597.

Del Genio, A. D., Y. Chen, D. Kim, and M. Yao, 2012: The MJO transition from shallow to deep convection in CloudSat/CALIPSO data and GISS GCM simulations. *J. Climate*, 25, 3755–3770.

Dudhia, J., 1989: Numerical study of convection observed during the winter monsoon experiment using a mesoscale two-dimensional model, *J. Atmos. Sci.*, 46, 3077–3107.

Hagos, S. and L. R. Leung, 2011: Moist thermodynamics of the Madden–Julian Oscillation in a cloud-resolving simulation. *J. Climate*, 24, 5571–5583.

——, Z. Feng, K. Landu, and C. N. Long, 2014: Advection, moistening, and shallow-to-deep convection transitions during the initiation and propagation of Madden-

Julian Oscillation, *J. Adv. Model. Earth Syst.*, 6, 938–949.

Hall, N. M. J., S. Thibaut, and P. Marchesiello, 2017: Impact of the observed extratropics on climatological simulations of the MJO in a tropical channel model. *Clim. Dyn.*, 48, 2541–2555.

Han J., H.-L. Pan, 2011: Revision of convection and vertical diffusion schemes in the NCEP Global Forecast System. *Wea. Forecasting*, 26, 520–533.

Hannah, W. M. and E. D. Maloney, 2011: The role of moisture–convection feedbacks in simulating the Madden–Julian oscillation. *J. Climate*, 24, 2754–2770.

Hendon, H.H. and M.L. Salby, 1994: The life cycle of the Madden–Julian oscillation. *J. Atmos. Sci.*, **51**, 2225–2237.

Hirota, N., T. Ogura, H. Tatebe, H. Shiogama, M. Kimoto, and M. Watanabe, 2018: Roles of shallow convective moistening in the eastward propagation of the MJO in MIROC6. *J. Climate,* 31, 3033–3047.

Hohenegger, C. and B. Stevens, 2013: Preconditioning deep convection with cumulus congestus. *J. Atmos. Sci.*, **70**, 448–464.

Holloway, C. E., and J. D. Neelin, 2009: Vertical structure, column water vapor, and tropical deep convection. *J. Atmos. Sci.*, **66**, 1665–1683.

Hong, S.-Y., J. Dudhia, and S.-H. Chen 2004: A revised approach to ice microphysical processes for the bulk parameterization of clouds and precipitation. *Mon. Wea. Rev.*, 132, 103–120.

——, Y. Noh, and J. Dudhia, 2006: A new vertical diffusion package with an explicit treatment of entrainment processes. *Mon. Wea. Rev.*, 134, 2318–2341.

Hsu, P. and T. Li, 2012: Role of the boundary layer moisture asymmetry in causing the eastward propagation of the Madden–Julian oscillation. *J. Climate*, 25, 4914–4931.

Huffman, G. J., R. F. Adler, M. M. Morrissey, D. T. Bolvin, S. Curtis, R. Joyce, B. McGavock, and J. Susskind, 2001: Global precipitation at one-degree daily resolution from multisatellite observations. *J. Hydrometeor.*, 2, 36–50.

Hung, M.-P., J.-L. Lin, W. Wang, D. Kim, T. Shinoda, and S. J. Weaver, 2013: MJO and convectively coupled equatorial waves simulated by CMIP5 climate models, *J. Clim.*, 26, 6185–6214.

Janiga, M. A. and C. Zhang, 2016: MJO moisture budget during DYNAMO in a cloud-resolving model. *J. Atmos. Sci.*, 73, 2257–2278.

Jiang, X., and Coauthors, 2015: Vertical structure and physical processes of the Madden-Julian oscillation: Exploring key model physics in climate simulations. *J. Geophys. Res. Atmos.*, 120, 4718–4748.

——, M. Zhao, E. D. Maloney, and D. E. Waliser, 2016: Convective moisture adjustment time scale as a key factor in regulating model amplitude of the Madden–Julian oscillation. *Geophys. Res. Lett.*, 43, 10412–10419.

Johnson, R.H. and P.E. Ciesielski, 2013: Structure and properties of Madden–Julian oscillations deduced from DYNAMO sounding arrays. *J. Atmos. Sci.*, 70, 3157–3179.

Kain, J. S., 2004: The Kain–Fritsch convective parameterization: An update. *J. Appl. Meteor.*, 43, 170–181.

Kemball-Cook, S. R., and B. C. Weare, 2001: The onset of convection in the Madden-

Julian oscillation. *J. Climate*, 14, 780–793.

Kikuchi, K., and Y. N. Takayabu, 2004: The development of organized convection associated with the MJO during TOGA COARE IOP: Trimodal characteristics. *Geophys. Res. Lett.*, 31, L10101.

Kim, D., A. H. Sobel, A. D. Del Genio, Y. Chen, S. J. Camargo, M. Yao, M. Kelley, and L. Nazarenko, 2012: The tropical subseasonal variability simulated in the NASA GISS general circulation model. *J. Climate*, 25, 4641–4659.

——, J.-S. Kug, and A. H. Sobel, 2014: Propagating versus nonpropagating Madden–Julian oscillation events. *J. Climate*, 27, 111–125.

Kumar, V. V., C. Jakob, A. Protat, P. T. May, and L. Davies, 2013: The four cumulus cloud modes and their progression during rainfall events: A C-band polarimetric radar perspective, *J. Geophys. Res. Atmos.*, 118, 8375–8389.

Lau, W. K.-M., and D. E. Waliser, 2012: Intraseasonal variability in the atmosphere-ocean climate system. Springer-Verlag, 614 pp.

Lee, H.-T., and NOAA CDR Program, 2011: NOAA Climate Data Record (CDR) of daily outgoing longwave radiation (OLR), Version 1.2. NOAA National Climatic Data Center.

Lin, J.-L., and Coauthors, 2006: Tropical intraseasonal variability in 14 IPCC AR4 climate models. Part I: Convective signals. *J. Climate*, 19, 2665–2690.

Ling, J. and C. Zhang, 2011: Structural evolution in heating profiles of the MJO in global reanalyses and TRMM retrievals. *J. Climate*, 24, 825–842.

Liu, Y., Z. Tan, and Z. Wu, 2019: Noninstantaneous wave-CISK for the interaction between convective heating and low-level moisture convergence in the tropics. *J. Atmos. Sci.*, 76, 2083–2101.

Ma, L. M., and Z.-M. Tan, 2009: Improving the behavior of the cumulus parameterization for tropical cyclone prediction: Convection trigger. *Atmos. Res.*, 92, 190–211.

Majda, A. J., and S. N. Stechmann, 2009: The skeleton of tropical intraseasonal oscillations. *Proc. Natl. Acad. Sci. USA*, 106, 8417–8422.

Maloney, E. D., 2009: The moist static energy budget of a composite tropical intraseasonal oscillation in a climate model. *J. Climate*, 22, 711–729.

Masunaga, H., 2013: A satellite study of tropical moist convection and environmental variability: A moisture and thermal budget analysis. *J. Atmos. Sci.*, 70, 2443–2466.

Matthews, A. J., and J. Lander, 1999: Physical and numerical contributions to the structure of Kelvin wave-CISK modes in a spectral transform model. *J. Atmos. Sci.*, 56, 4050–4058.

Monin, A. S., and A. M. Obukhov, 1954: Basic laws of turbulent mixing in the surface layer of the atmosphere, *Contrib. Geophys. Inst. Acad. Sci.*, USSR, 151, 163–187.

Mlawer, E. J., S. J. Taubman, P. D. Brown, M. J. Iacono, and S. A. Clough, 1997: Radiativetransfer for inhomogeneous atmosphere: RRTM, a validated correlated‐k model for the longwave, *J. Geophys. Res.*, 102, 16663–16682.

Pilon, R., C. Zhang, and J. Dudhia, 2016: Roles of deep and shallow convection and microphysics in the MJO simulated by the Model for Prediction Across Scales, *J. Geophys. Res. Atmos.*, 121, 10575–10600.

Powell, S. W., and R. A. Houze Jr., 2015: Effect of dry large-scale vertical motions on initial MJO convective onset. *J. Geophys. Res. Atmos.*, 120, 4783–4805.

Ray, P., C. Zhang, J. Dudhia, and S. S. Chen, 2009: A numerical case study on the initiation of the Madden–Julian oscillation. *J. Atmos. Sci.*, 66, 310–331.

——, C. Zhang, M. Moncrieff, J. Dudhia, J. Caron, L. Leung, and C. Bruyère, 2011: Role of the atmospheric mean state on the initiation of the MJO in a tropical channel model. *Clim. Dyn.*, 36. 161–184.

Raymond, D. J., and Z. Fuchs, 2009: Moisture modes and the Madden–Julian oscillation. *J. Climate*, 22, 3031–3046.

Reynolds, R. W., T. M. Smith, C. Liu, D. B. Chelton, K. S. Casey, and M. G. Schlax, 2007: Daily high-resolution-blended analyses for sea surface temperature. *J. Climate*, 20, 5473–5496.

Riley, E.M., B.E. Mapes, and S.N. Tulich, 2011: Clouds associated with the Madden–Julian oscillation: A new perspective from CloudSat. *J. Atmos. Sci.*, 68, 3032–3051.

Rowe, A. K., and R. A. Houze Jr., 2015: Cloud organization and growth during the transition from suppressed to active MJO conditions, *J. Geophys. Res. Atmos.*, 120, 10, 324–10, 350.

Ruppert, J. H., Jr., and R. H. Johnson, 2015: Diurnally modulated cumulus moistening in the pre-onset stage of the Madden–Julian oscillation during DYNAMO. *J. Atmos. Sci.*, 72, 1622–1647.

Skamarock, W. C., and Coauthors, 2008: A description of the Advanced Research WRF version 3. NCAR Tech. Note NCAR/TN-4751STR, 113 pp., https://doi.org/10.5065/D68S4MVH.

Sobel, A., and E. Maloney, 2012: An idealized semi-empirical framework for modeling the Madden-Julian Oscillation. *J. Atmos. Sci.*, 69, 1691–1705.

Suhas, E., and G. J. Zhang, 2015: Evaluating convective parameterization closures using cloud-resolving model simulation of tropical deep convection, *J. Geophys. Res. Atmos.*, 120, 1260–1277.

Tokioka, T., K. Yamazaki, A. Kitoh, and T. Ose, 1988: The equatorial 30–60 day oscillation and the Arakawa-Schubert penetrative cumulus parameterization, *J. Meteor. Soc. Japan*, 66, 883–901.

Ulate, M., C. Zhang, and J. Dudhia, 2015: Role of water vapor and convection-circulation decoupling in MJO simulations by a tropical channel model. *J. Adv. Model. Earth Syst.*, 7, 692–711.

Wang, B., and H. Rui, 1990: Dynamics of the coupled moist Kelvin–Rossby wave on an equatorial b-plane. *J. Atmos. Sci.*, 47, 397–413.

Wheeler, M., and G. N. Kiladis, 1999: Convectively coupled equatorial waves: Analysis of clouds and temperature in the wavenumber–frequency domain. *J. Atmos. Sci.*, 56, 374–399.

Wu, Z., E. S. Sarachik, and D. S. Battisti, 2000: Vertical structure of convective heating and the three-dimensional structure of the forced circulation on an equatorial beta plane. *J. Atmos. Sci.*, 57, 2169–2187.

——, 2003: A shallow CISK, deep equilibrium mechanism for the interaction between large-scale convection and large-scale circulations in the tropics, *J. Atmos. Sci.*, 60, 377–392.

Xu, W., and S. A. Rutledge, 2016: Time scales of shallow-to-deep convective transition associated with the onset of Madden-Julian Oscillations, *Geophys. Res. Lett.*, 43, 2880–2888.

Yanai, M., S. Esbensen, and J.-H. Chu, 1973: Determination of bulk properties of tropical cloud clusters from large-scale heat and moisture budgets, *J. Atmos. Sci.*, 30, 611–627.

Zhang, C., 2005: Madden-Julian oscillation. *Rev. Geophys.*, 43, RG2003.

——, 2013: Madden-Julian oscillation: Bridging weather and climate. *Bull. Amer. Meteor. Soc.*, 94, 1849–1870.

Zhang, C., and Y. Wang, 2017: Projected future changes of tropical cyclone activity over the western North and South Pacific in a 20-km-Mesh regional climate model. *J. Climate*, 30, 5923–5941.

Zhu, H., and H. H. Hendon, 2015: Role of large scale moisture advection for simulation of the MJO with increased entrainment. *Quart. J. Roy. Meteor. Soc.*, 141, 2127–2136.

Table captions

Table 1. Summary of criteria and closure assumptions for shallow convection in 3 cumulus parameterization schemes used in this study. P_s is the surface pressure. D_{min} is the minimum cloud depth, which is a function of the temperature of lifting condensation level.

Tables

CP schemes	Criteria for shallow convection	Closure assumptions for shallow convection (cloud-base mass flux)
Simplified Arakawa-Schubert (**SAS**)	Cloud depth ≤ 150 hPa, cloud top pressure ≥ $0.7P_s$	Related to surface buoyancy flux
Tiedtke (**TDK**)	Cloud depth ≤ 200 hPa	Related to tendency of boundary layer moist static energy
Kain-Fritsch with trigger (**KFMT**)	Cloud depth ≤ D_{min}, D_{min} varies from 2 km to 4 km	Related to subcloud layer turbulent kinetic energy

Table 1. Summary of criteria and closure assumptions for shallow convection in 3 cumulus parameterization schemes used in this study. P_s is the surface pressure. D_{min} is the minimum cloud depth, which is a function of the temperature of lifting condensation level.

Figure captions

Figure 1. Boreal winter-mean precipitation (mm d^{-1}) in observation (a) and simulations with CP schemes of SAS (b), TDK (d) and KF (f). The difference of boreal winter-mean precipitation (mm d^{-1}) between simulations of SAS-n and SAS (c), TDK-n and TDK (e), KF-n and KF (g).

Figure 2. Boreal winter variance of MJO-filtered (periods 20-100 days, eastward propagating wavenumbers 1-5) precipitation (mm^2 d^{-2}) in observation (a) and simulations with CP schemes of SAS (b), SAS-n (c), TDK (d), TDK-n (e), and KF (f) and KF-n (g).

Figure 3. Longitude-time evolution of OLR anomalies by lag correlations of 20-100 day band-pass-filtered anomalous OLR with itself averaged over the equatorial Indian Ocean box (80-90°E; 5°S-5°N). (a) is for observation and (b)-(g) are for simulations with different CP schemes. Fields are averaged between 10°S and 10°N. Solid lines in each panel denote the eastward propagation speed of 8 m s^{-1}.

Figure 4. Frequency-zonal wavenumber power spectra of the symmetric component (about the equator) of OLR for (a) observation and (b)-(g) simulations with different CP schemes. Shaded is the base-10 logarithm of the averaged power between 15°S and 15°N.

Figure 5. Longitude-time evolution of specific humidity anomalies (g kg^{-1}, shading) and 850 hPa zonal wind anomalies (contours, interval of 0.3 m s^{-1}, positive, zero and negative values represented by thin dashed, thick solid and thin solid lines) by lag regression of 20-100 day band-pass-filtered anomalous specific humidity and

zonal wind against Indian Ocean precipitation (80-90°E; 5°S-5°N). (a) is for observation and (b)-(g) are for simulations with different CP schemes. Regression is scaled to 3 mm d^{-1} precipitation rate. Fields are averaged between 10°S and 10°N. Solid straight lines in each panel denote the eastward propagation speed of 8 m s^{-1}.

Figure 6. Time-height structures of diabatic heating anomalies (K) by lag regression of 20-100 day band-pass-filtered anomalous total diabatic heating at the longitude of 90°E against Indian Ocean precipitation (80-90°E; 5°S-5°N). (a) is for observation and (b)-(g) are for simulations with different CP schemes. Thick solid lines represent zero heating anomaly. Regression is scaled to 3 mm d^{-1} precipitation rate. Fields are averaged between 10°S and 10°N.

Figure 7. As in Fig. 6, but for the mass convergence term (10^{-6} g kg^{-1} s^{-1}) in Eq. (3).

Figure 8. As in Fig. 6, but for the horizontal moisture advection term (10^{-6} g kg^{-1} s^{-1}) in Eq. (3).

Figure 9. Time evolution of diabatic heating (K, red line) and moisture divergence (10^{-6} g kg^{-1} s^{-1}, sign reversed moisture convergence, blue line) anomalies by lag regression of 20-100 day band-pass-filtered anomalous of 850-hPa total diabatic heating and 925-hPa moisture convergence at the longitude of 90°E against Indian Ocean precipitation (80-90°E; 5°S-5°N). (a) is for observation and (b)-(d) are for simulations with different CP schemes. In (b)-(d), solid and dashed lines represent original and modified schemes respectively. Regression is scaled to 3 mm d^{-1} precipitation rate. Fields are averaged between 10°S and 10°N.

Figure 10. Horizontal patterns of moisture convergence (10^{-6} g kg^{-1} s^{-1}) and horizontal wind anomalies calculated by zero lag-regression of 20-100 day band-pass-filtered anomalous 925-hPa moisture convergence and 850-hPa horizontal wind against Indian Ocean precipitation (80-90°E; 5°S-5°N). (a) is for observation and (b)-(d) are for simulations with different CP schemes. Regression is scaled to 3 mm d^{-1} precipitation rate.

Figure 11. Longitude-height structures of specific humidity (g kg^{-1}) calculated by zero lag-regression of 20-100 day band-pass-filtered anomalous specific humidity against Indian Ocean precipitation (80-90°E; 5°S-5°N). (a) is for observation and (b)-(g) are for simulations with different CP schemes. Regression is scaled to 3 mm d^{-1} precipitation rate. Fields are averaged between 10°S and 10°N.

Figure 12. Horizontal patterns of the differences of moisture convergence terms (10^{-6} g kg^{-1} s^{-1}) between 3 pairs of simulations with different CP schemes, calculated by zero lag-regression of 20-100 day band-pass-filtered anomalous 925-hPa mass convergence (a, c, e) and moisture advection (b, d, f) against Indian Ocean precipitation (80-90°E; 5°S-5°N). Regression is scaled to 3 mm d^{-1} precipitation rate.

Figure 13. Longitude-height structures of moisture advection (10^{-6} g kg^{-1} s^{-1}) calculated by zero lag-regression of 20-100 day band-pass-filtered anomalous horizontal moisture advection against Indian Ocean precipitation (80-90°E; 5°S-5°N). (a) is for observation and (b), (d), (f) are for simulations with SAS, TDK, and KF schemes respectively. (c), (e), (g) are the differences between 3 pairs of

simulations. Regression is scaled to 3 mm d^{-1} precipitation rate. Fields are averaged between 10°S and 10°N.

Figure 14. As in Fig. 13 (c), (e) and (g), but for the zonal (a, c, e) and meridional (b, d, f) moisture advection (10^{-6} g kg^{-1} s^{-1}).

Figure 15. Ratio number (occurrence times averaged by total time steps and the number of horizontal grids in the region of 60-180°E, 15°S-15°N) change for shallow (circle) and deep (triangle) convection in 3 pairs of simulations with different CP schemes.

Figures

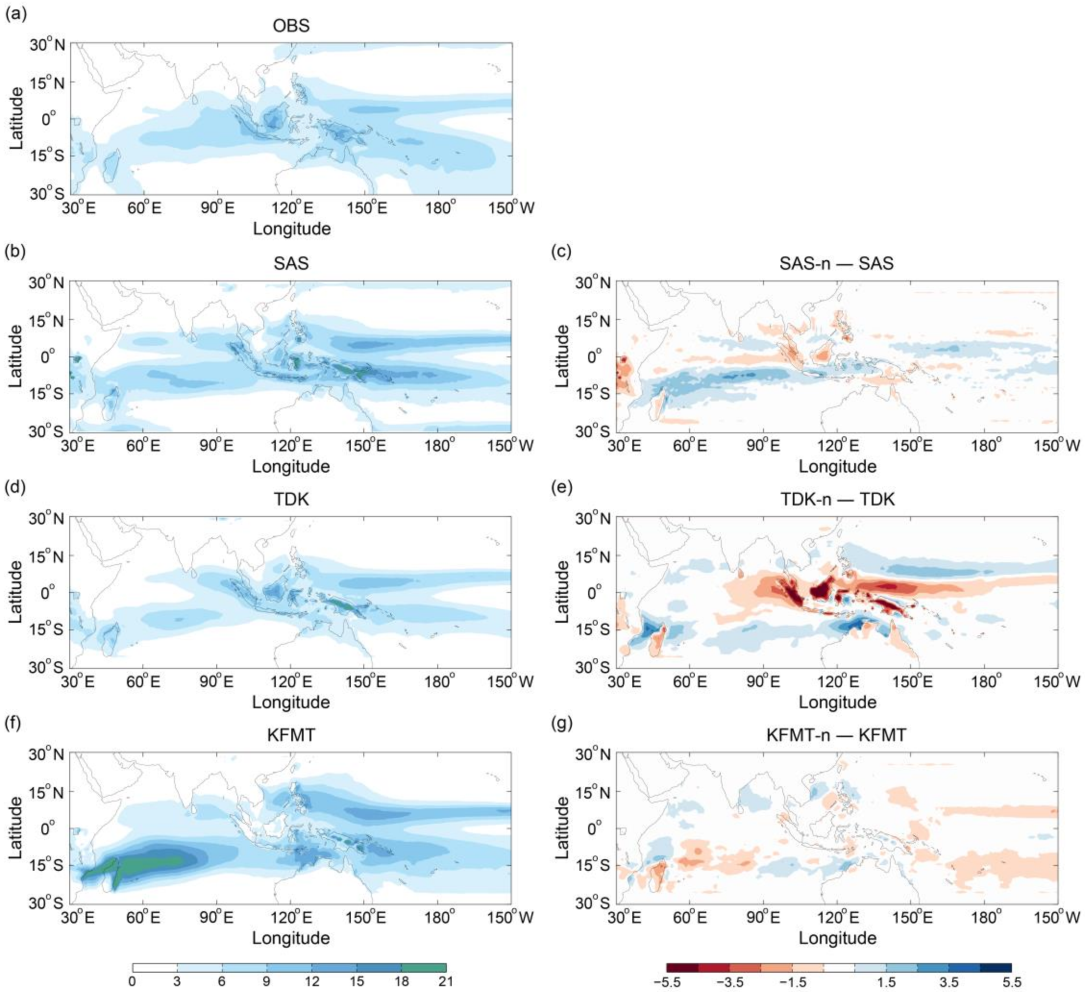

Figure 1. Boreal winter-mean precipitation (mm d^{-1}) in observation (a) and simulations with CP schemes of SAS (b), TDK (d) and KFMT (f). The difference of boreal winter-mean precipitation (mm d^{-1}) between simulations of SAS-n and SAS (c), TDK-n and TDK (e), KFMT-n and KFMT (g).

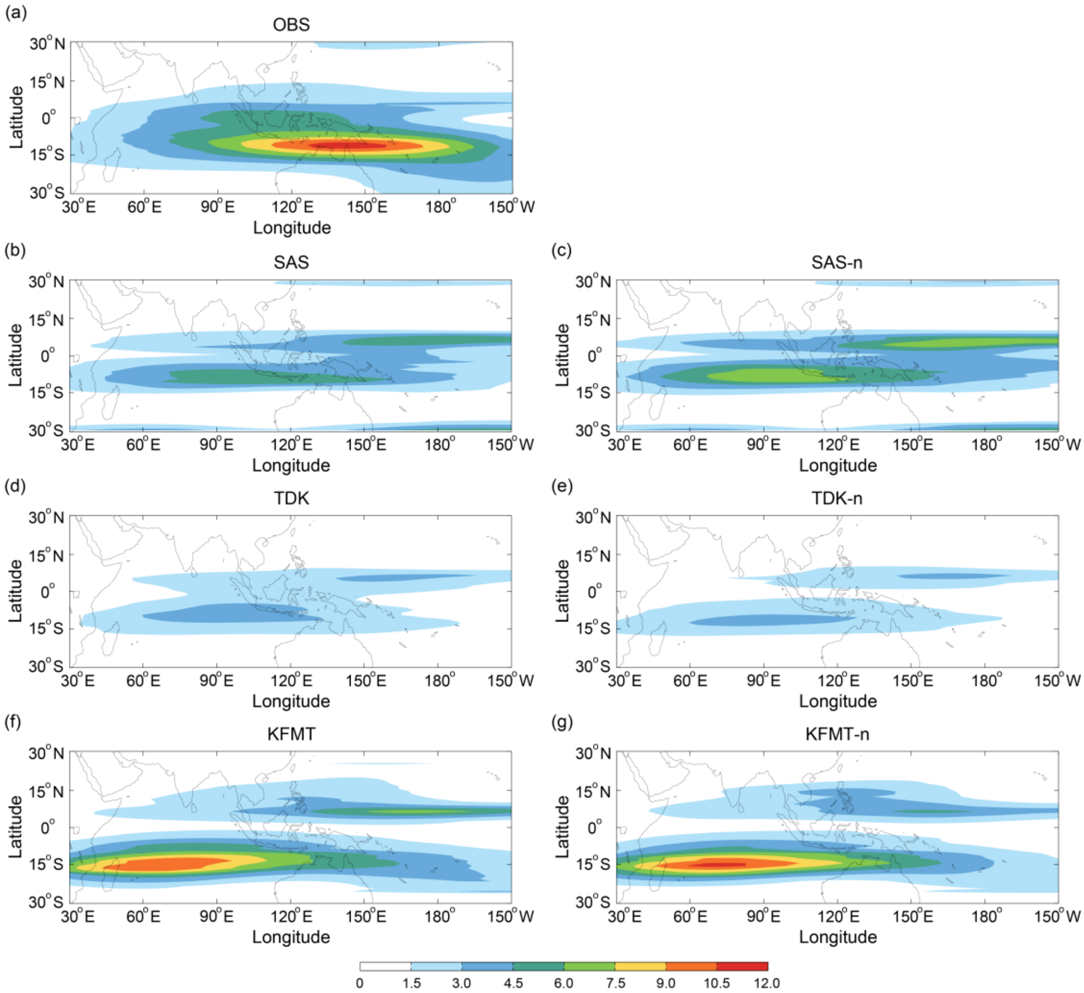

Figure 2. Boreal winter variance of MJO-filtered (periods 20-100 days, eastward propagating wavenumbers 1-5) precipitation (mm^2 d^{-2}) in observation (a) and simulations with CP schemes of SAS (b), SAS-n (c), TDK (d), TDK-n (e), KFMT (f) and KFMT-n (g).

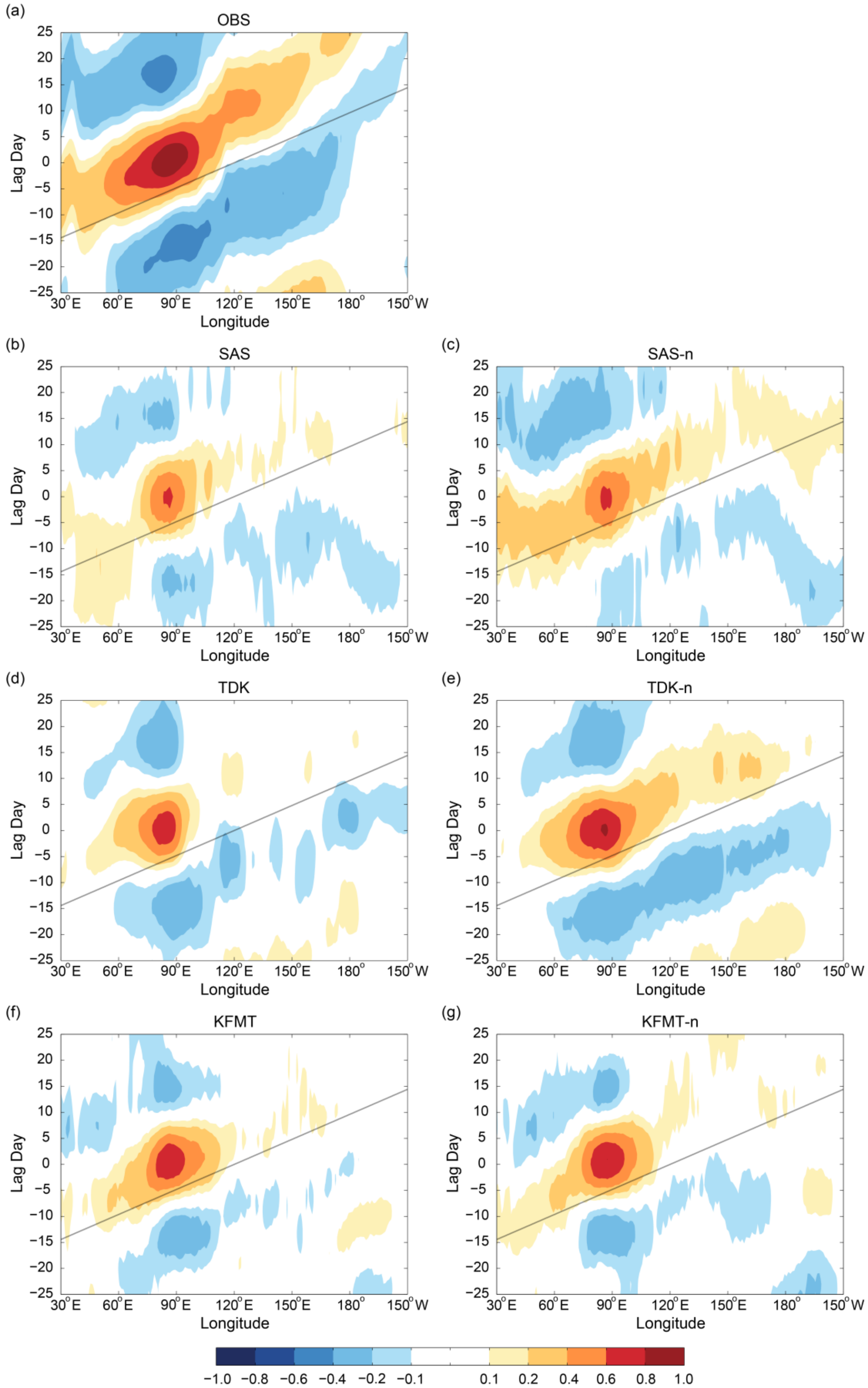
(a)
OBS
(b)
SAS
(c)
SAS-n
(d)
TDK
(e)
TDK-n
(f)
KFMT
(g)
KFMT-n
Lag Day
Longitude
25 20 15 10 5 0 −5 −10 −15 −20 −25
30°E 60°E 90°E 120°E 150°E 180° 150°W
−1.0 −0.8 −0.6 −0.4 −0.2 −0.1 0.1 0.2 0.4 0.6 0.8 1.0

Figure 3. Longitude-time evolution of OLR anomalies by lag correlations of 20-100 day band-pass-filtered anomalous OLR with itself averaged over the equatorial Indian Ocean box (80-90°E; 5°S-5°N). (a) is for observation and (b)-(g) are for simulations with different CP schemes. Fields are averaged between 10°S and 10°N. Solid lines in each panel denote the eastward propagation speed of 8 m s^{-1}.

796

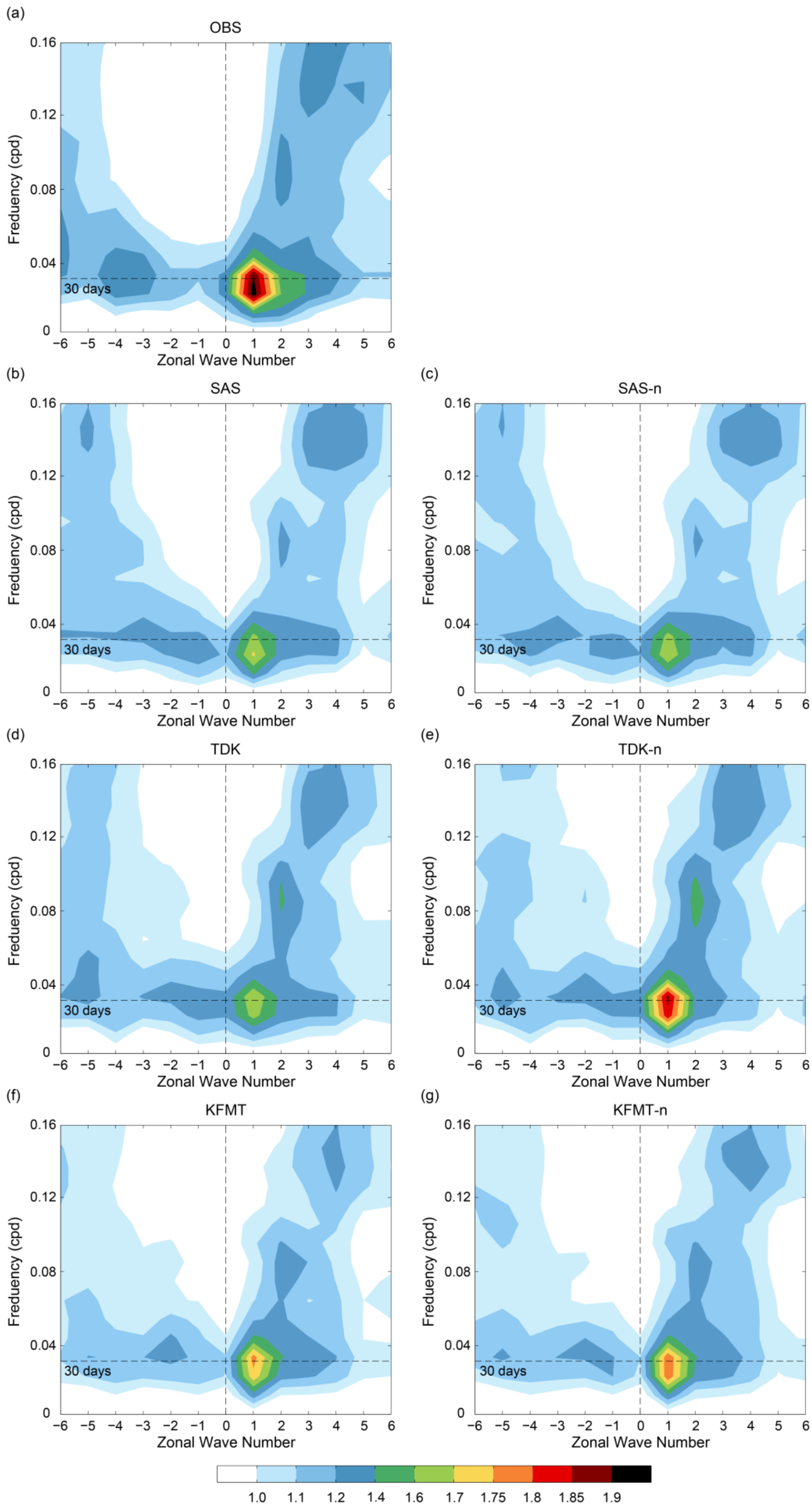

(a)
OBS
(b)
SAS
(c)
SAS-n
(d)
TDK
(e)
TDK-n
(f)
KFMT
(g)
KFMT-n
Frequency (cpd)
Zonal Wave Number
30 days
1.0
1.1
1.2
1.4
1.6
1.7
1.75
1.8
1.85
1.9

Figure 4. Frequency-zonal wavenumber power spectra of the symmetric component (about the equator) of OLR for (a) observation and (b)-(g) simulations with different CP schemes. Shaded is the base-10 logarithm of the averaged power between 15°S and 15°N.

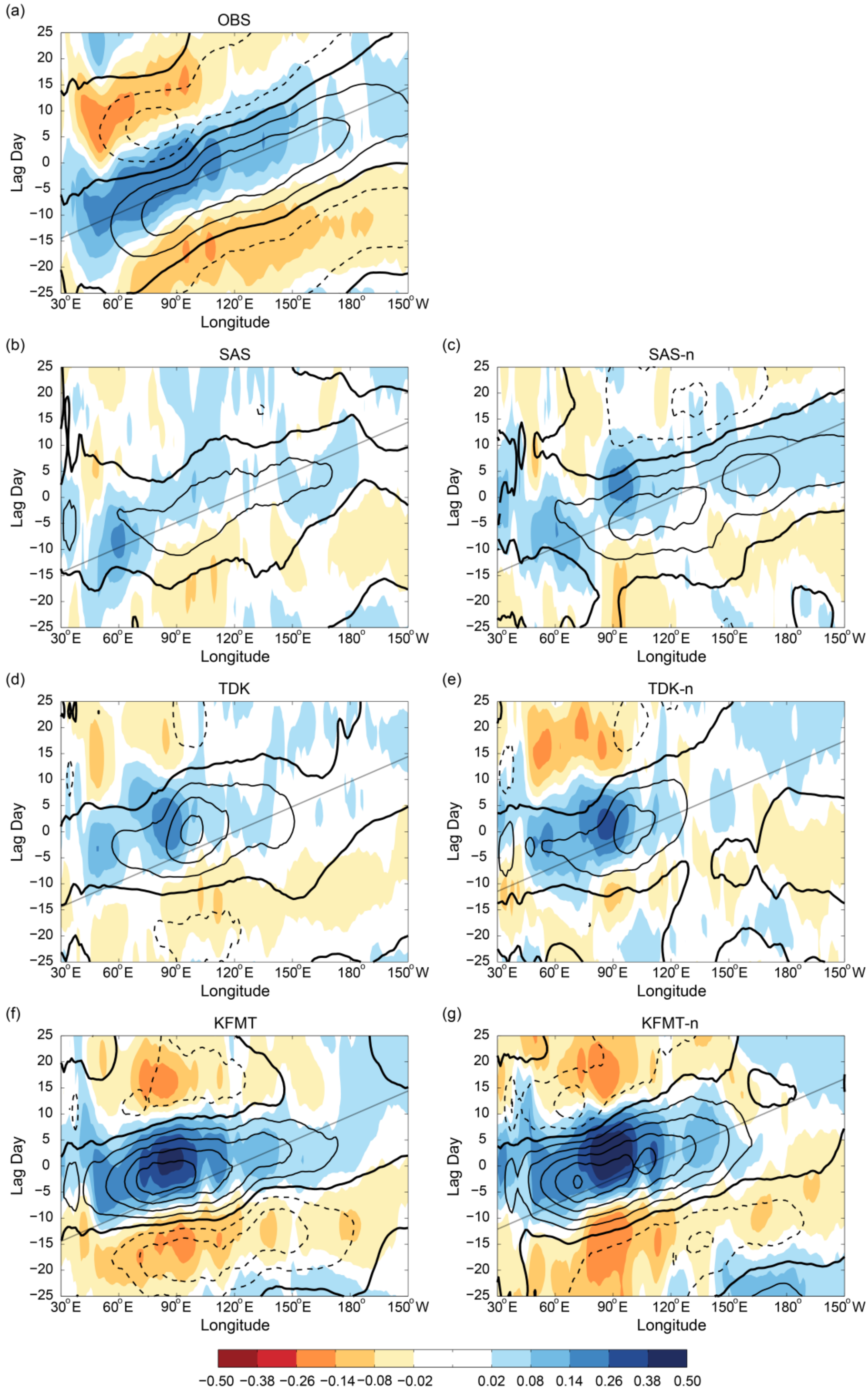
(a)
OBS
(b)
SAS
(c)
SAS-n
(d)
TDK
(e)
TDK-n
(f)
KFMT
(g)
KFMT-n
Lag Day
Longitude
25
20
15
10
5
0
−5
−10
−15
−20
−25
30°E
60°E
90°E
120°E
150°E
180°
150°W
−0.50 −0.38 −0.26 −0.14 −0.08 −0.02
0.02 0.08 0.14 0.26 0.38 0.50

Figure 5. Longitude-time evolution of specific humidity anomalies (g kg^{-1}, shading) and 850 hPa zonal wind anomalies (contours, interval of 0.3 m s^{-1}, positive, zero and negative values represented by thin dashed, thick solid and thin solid lines) by lag regression of 20-100 day band-pass-filtered anomalous specific humidity and zonal wind against Indian Ocean precipitation (80-90°E; 5°S-5°N). (a) is for observation and (b)-(g) are for simulations with different CP schemes. Regression is scaled to 3 mm d^{-1} precipitation rate. Fields are averaged between 10°S and 10°N. Solid straight lines in each panel denote the eastward propagation speed of 8 m s^{-1}.

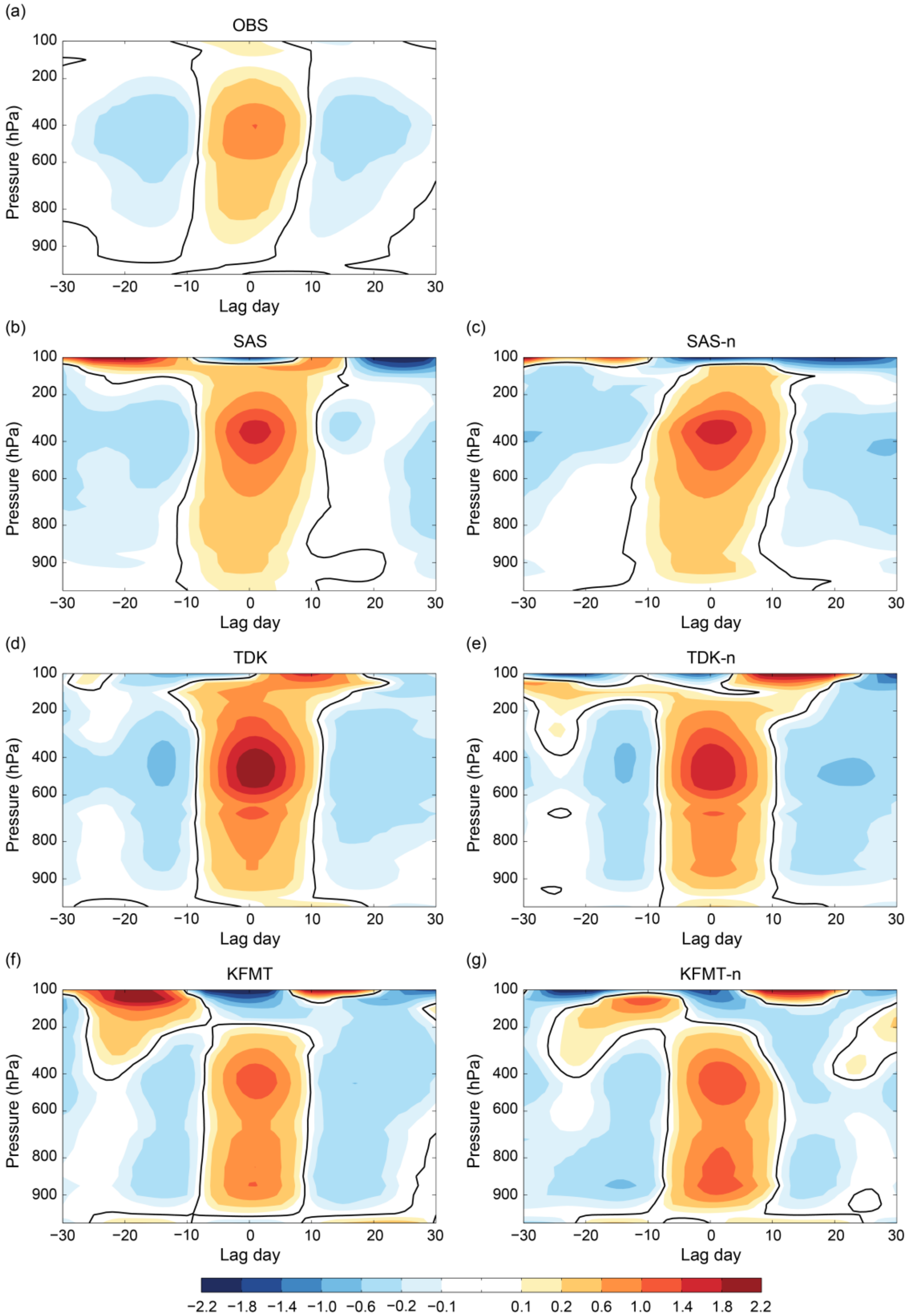
(a)
OBS
(b)
SAS
(c)
SAS-n
(d)
TDK
(e)
TDK-n
(f)
KFMT
(g)
KFMT-n
Pressure (hPa)
Lag day
100
200
400
600
800
900
−30
−20
−10
0
10
20
30
−2.2
−1.8
−1.4
−1.0
−0.6
−0.2
−0.1
0.1
0.2
0.6
1.0
1.4
1.8
2.2

812

Figure 6. Time-height structures of diabatic heating anomalies (K) by lag regression of 20-100 day band-pass-filtered anomalous total diabatic heating at the longitude of 90°E against Indian Ocean precipitation (80-90°E; 5°S-5°N). (a) is for observation and (b)-(g) are for simulations with different CP schemes. Thick solid lines represent zero heating anomaly. Regression is scaled to 3 mm d^{-1} precipitation rate. Fields are averaged between 10°S and 10°N.

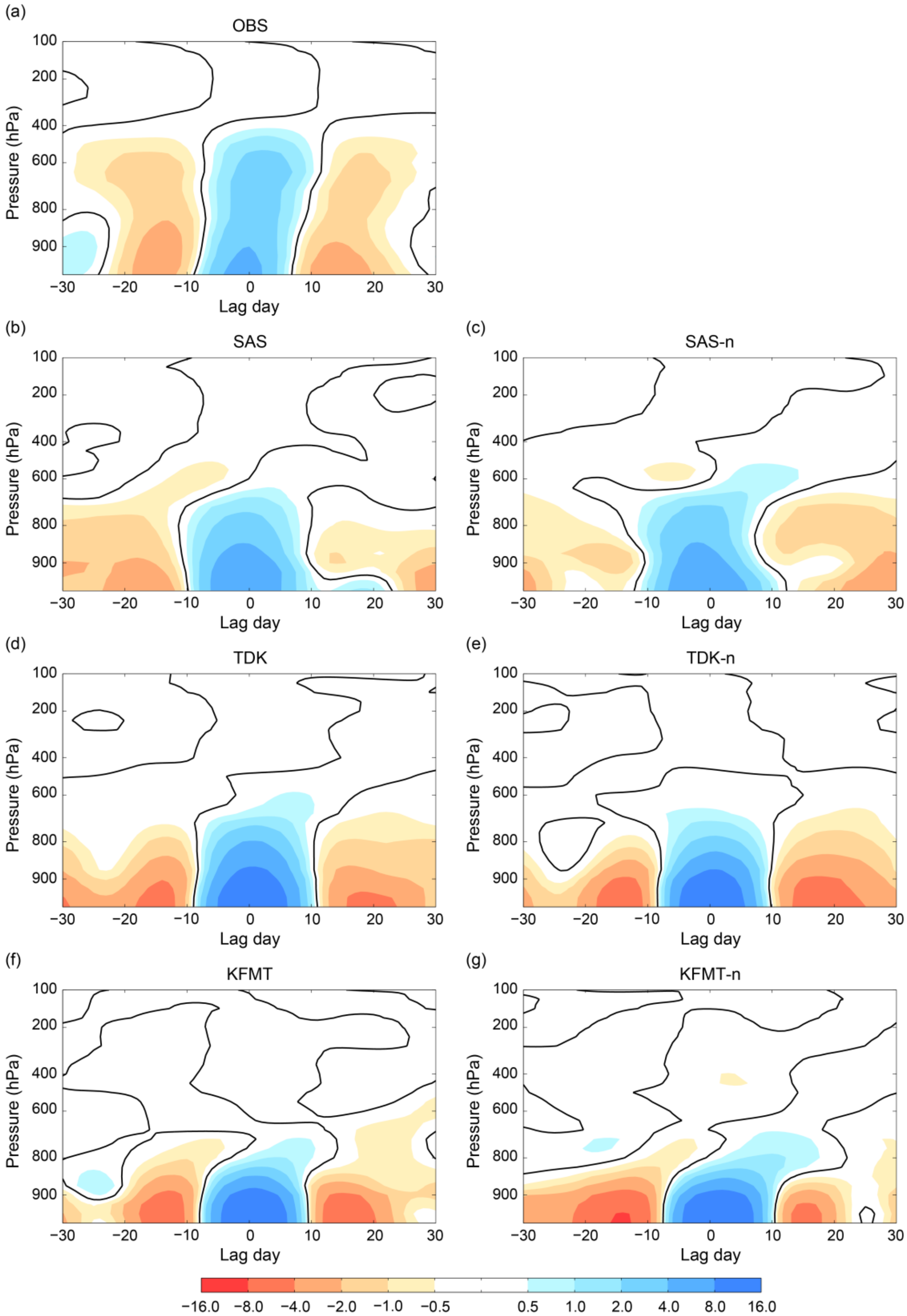

Figure 7. As in Fig. 6, but for the mass convergence term (10^{-6} g kg^{-1} s^{-1}) in Eq. (3).

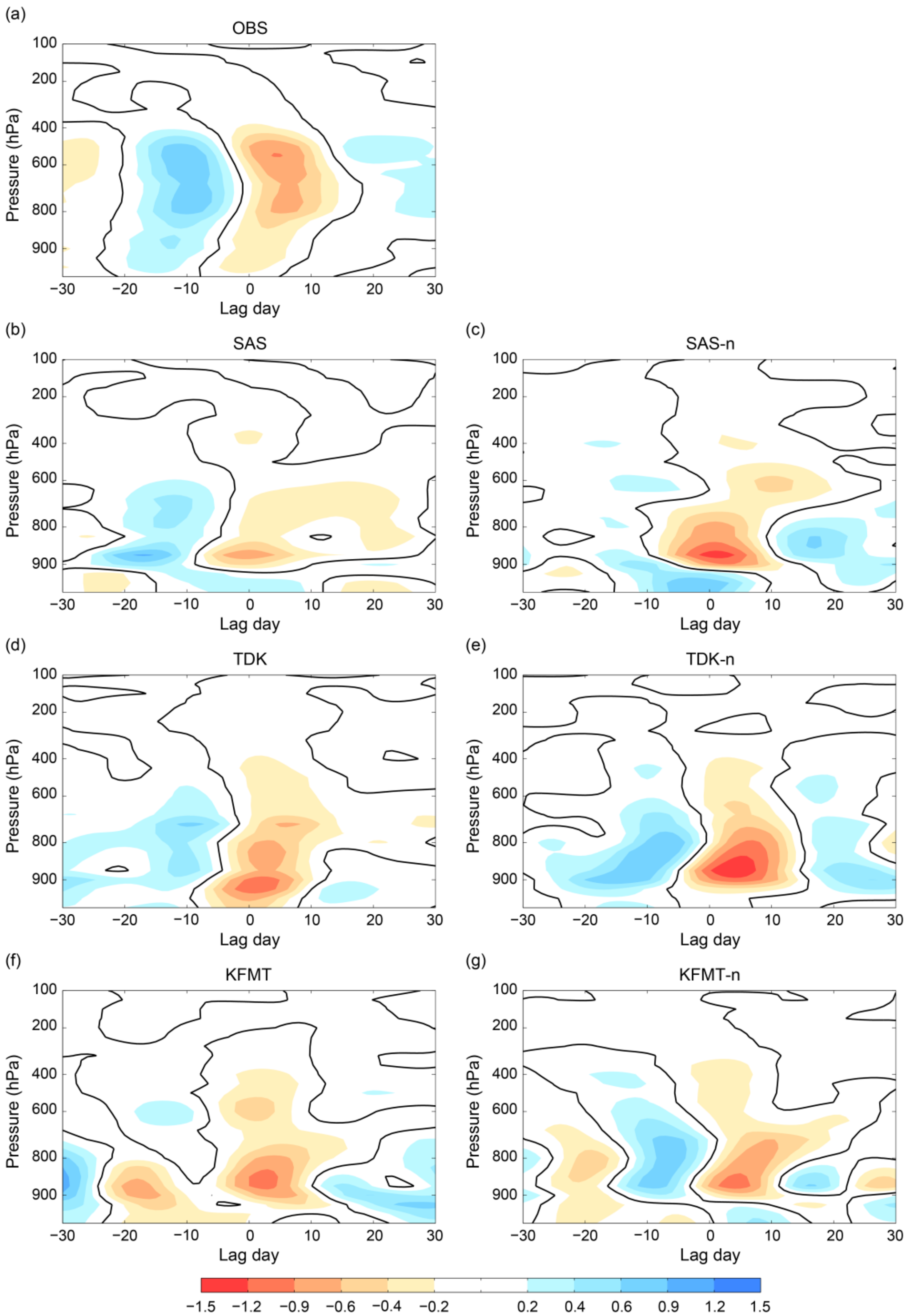

Figure 8. As in Fig. 6, but for the horizontal moisture advection term (10^{-6} g kg^{-1} s^{-1}) in Eq. (3).

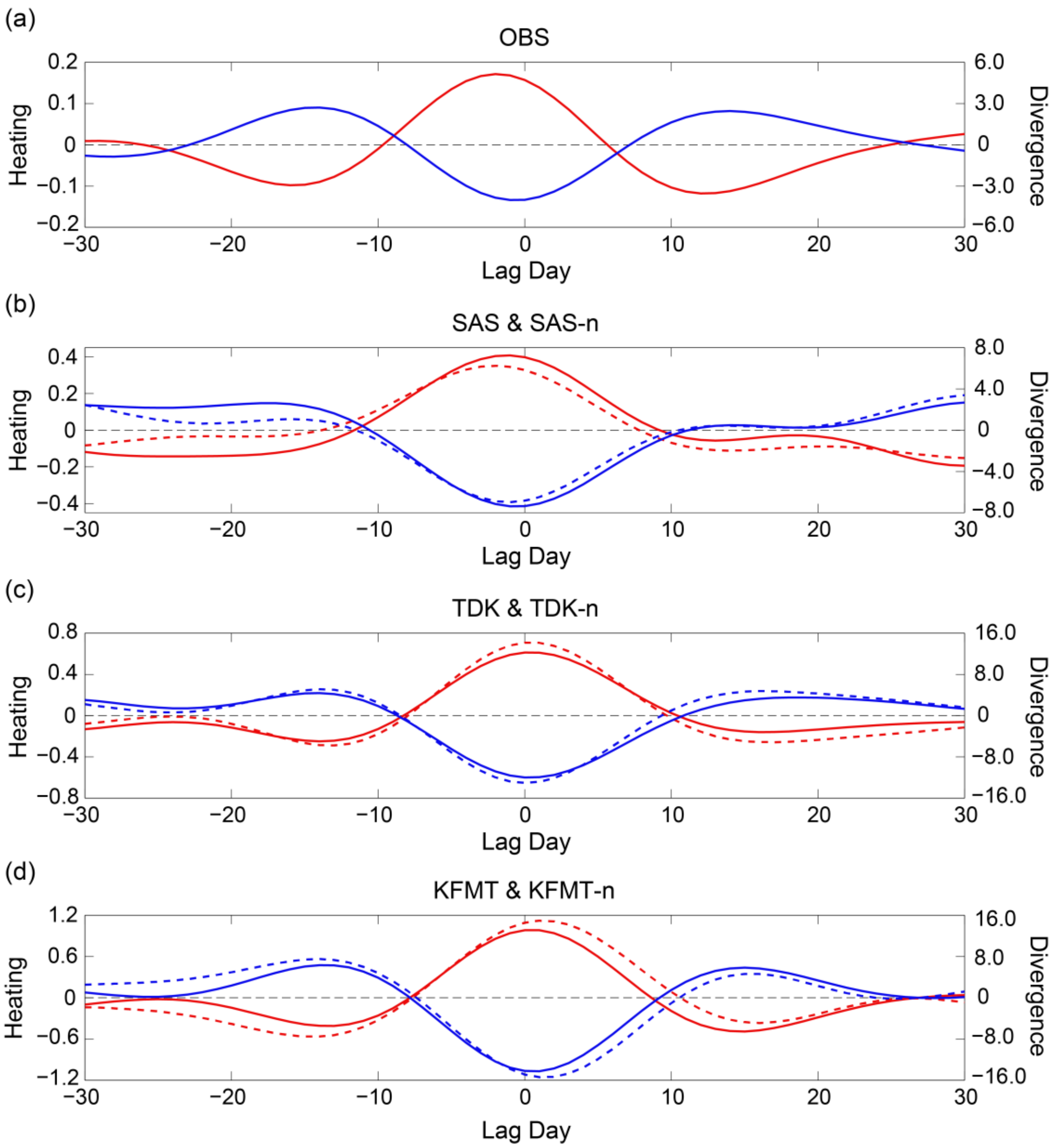
(a)
OBS
Heading
Divergence
Lag Day
0.2
0.1
0
−0.1
−0.2
6.0
3.0
0
−3.0
−6.0
−30
−20
−10
0
10
20
30
(b)
SAS & SAS-n
Heating
Divergence
Lag Day
0.4
0.2
0
−0.2
−0.4
8.0
4.0
0
−4.0
−8.0
(c)
TDK & TDK-n
Heating
Divergence
Lag Day
0.8
0.4
0
−0.4
−0.8
16.0
8.0
0
−8.0
−16.0
(d)
KFMT & KFMT-n
Heating
Divergence
Lag Day
1.2
0.6
0
-0.6
-1.2
16.0
8.0
0
−8.0
−16.0

Figure 9. Time evolution of diabatic heating (K, red line) and moisture divergence (10^{-6} g kg^{-1} s^{-1}, sign reversed moisture convergence, blue line) anomalies by lag regression of 20-100 day band-pass-filtered anomalous of 850-hPa total diabatic heating and 925-hPa moisture convergence at the longitude of 90°E against Indian Ocean precipitation (80-90°E; 5°S-5°N). (a) is for observation and (b)-(d) are for simulations with different CP schemes. In (b)-(d), solid and dashed lines represent original and modified schemes respectively. Regression is scaled to 3 mm d^{-1} precipitation rate. Fields are averaged between 10°S and 10°N.

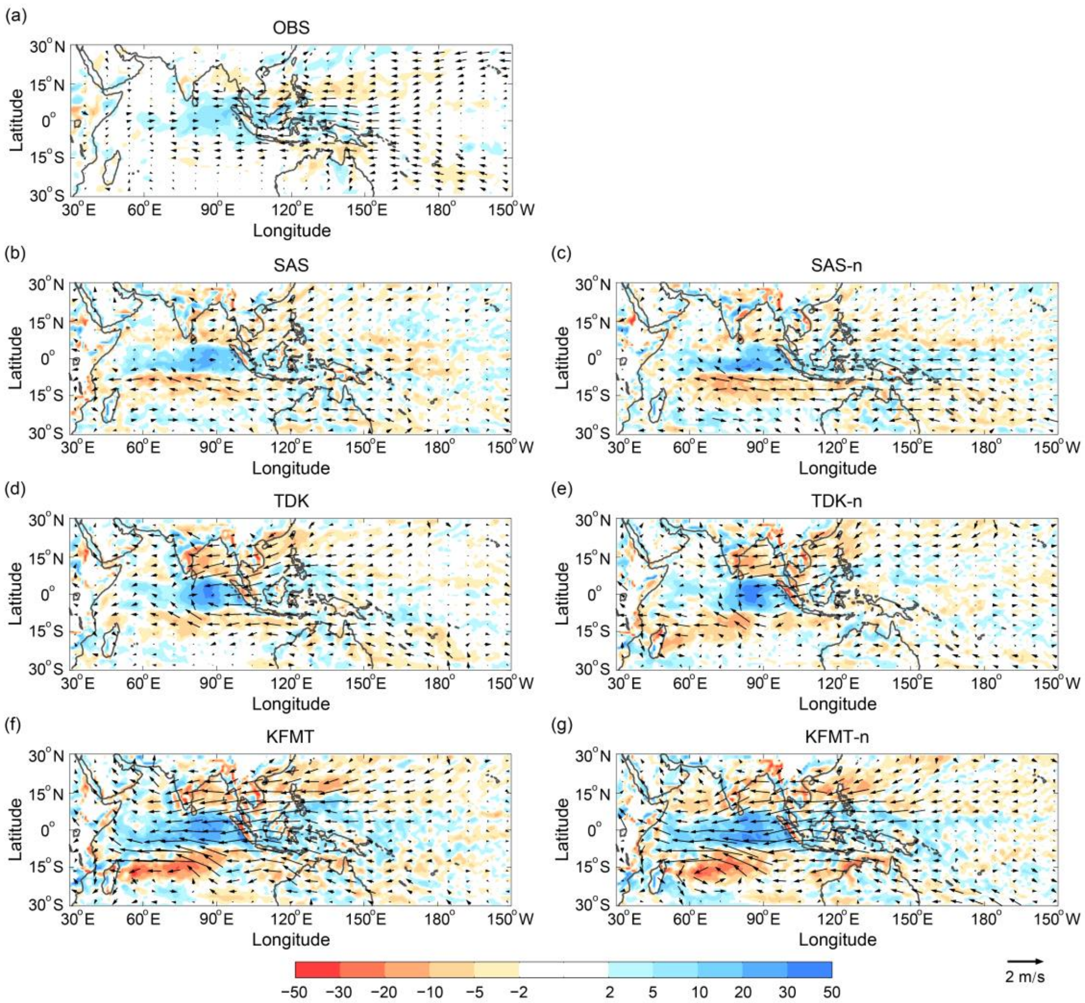

Figure 10. Horizontal patterns of moisture convergence (10^{-6} g kg^{-1} s^{-1}) and horizontal wind anomalies calculated by zero lag-regression of 20-100 day band-pass-filtered anomalous 925-hPa moisture convergence and 850-hPa horizontal wind against Indian Ocean precipitation (80-90°E; 5°S-5°N). (a) is for observation and (b)-(g) are for simulations with different CP schemes. Regression is scaled to 3 mm d^{-1} precipitation rate.

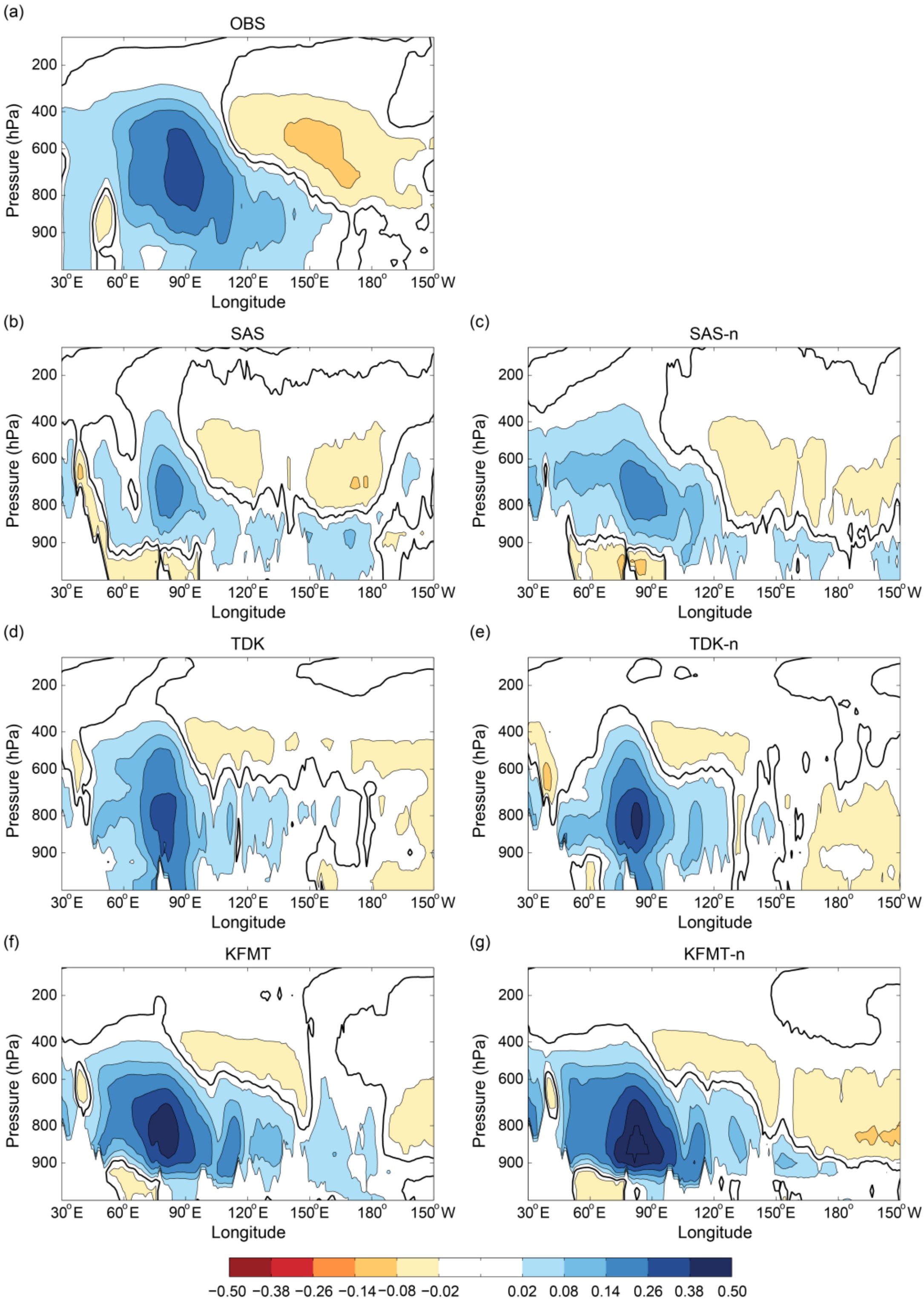

(a)
OBS
(b)
SAS
(c)
SAS-n
(d)
TDK
(e)
TDK-n
(f)
KFMT
(g)
KFMT-n
Pressure (hPa)
200
400
600
800
900
30°E 60°E 90°E 120°E 150°E 180° 150°W
Longitude
−0.50 −0.38 −0.26 −0.14 −0.08 −0.02 0.02 0.08 0.14 0.26 0.38 0.50

Figure 11. Longitude-height structures of specific humidity (g kg^{-1}) calculated by zero lag-regression of 20-100 day band-pass-filtered anomalous specific humidity against Indian Ocean precipitation (80-90°E; 5°S-5°N). (a) is for observation and (b)-(g) are for simulations with different CP schemes. Regression is scaled to 3 mm d^{-1} precipitation rate. Fields are averaged between 10°S and 10°N.

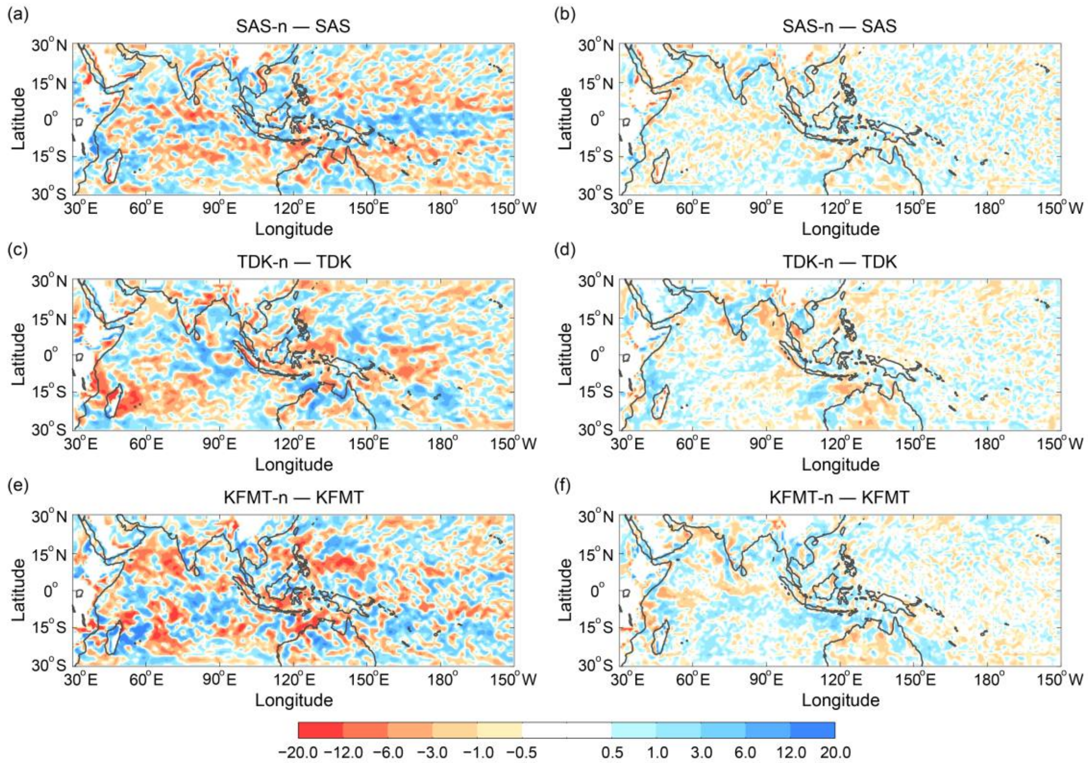

Figure 12. Horizontal patterns of the differences of moisture convergence terms (10^{-6} g kg^{-1} s^{-1}) between 3 pairs of simulations with different CP schemes, calculated by zero lag-regression of 20-100 day band-pass-filtered anomalous 925-hPa mass convergence (a, c, e) and moisture advection (b, d, f) against Indian Ocean precipitation (80-90°E; 5°S-5°N). Regression is scaled to 3 mm d^{-1} precipitation rate.

859

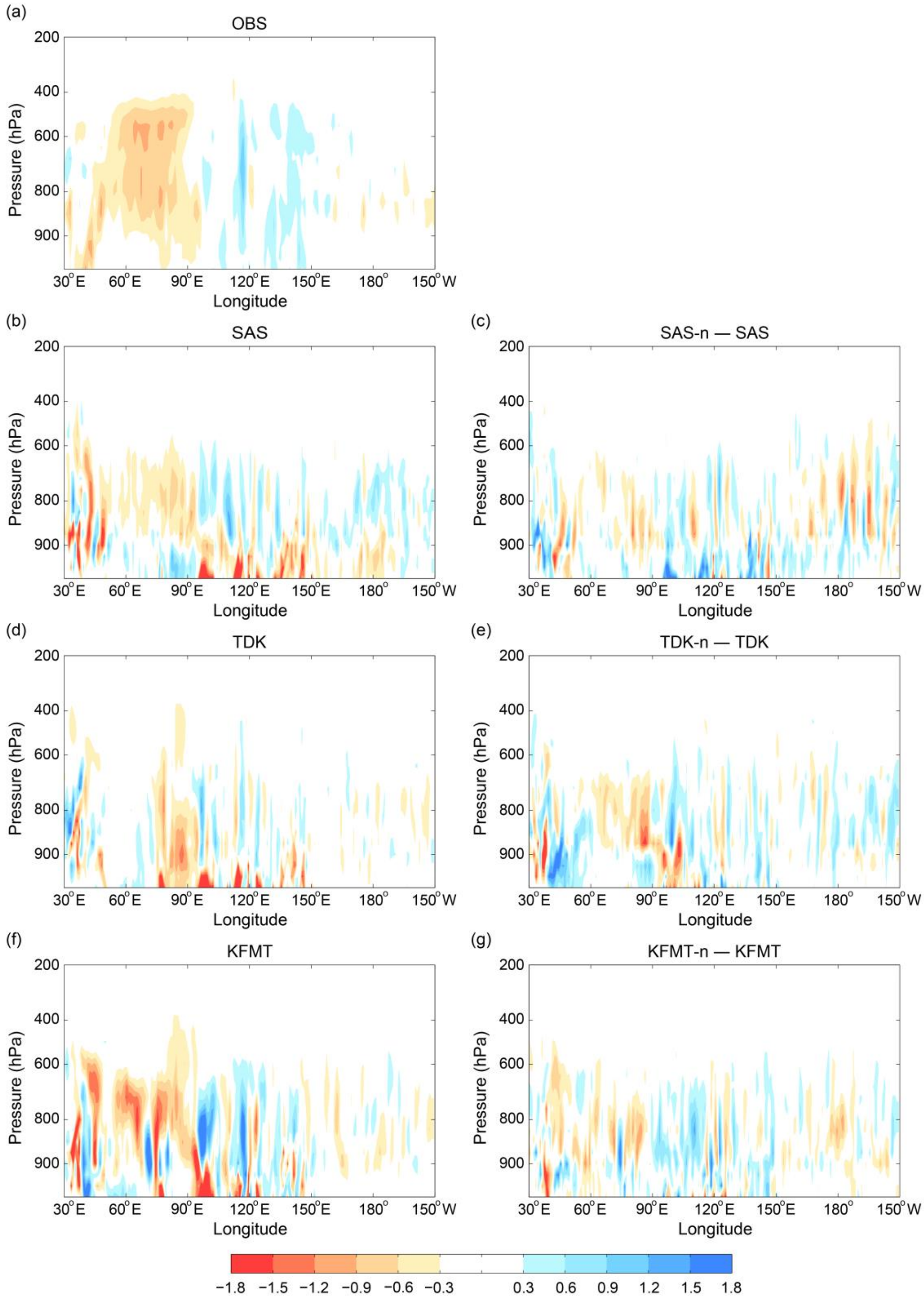

(a)
OBS
(b)
SAS
(c)
SAS-n — SAS
(d)
TDK
(e)
TDK-n — TDK
(f)
KFMT
(g)
KFMT-n — KFMT
Pressure (hPa)
200
400
600
800
900
30°E
60°E
90°E
120°E
150°E
180°
150°W
Longitude
−1.8 −1.5 −1.2 −0.9 −0.6 −0.3 0.3 0.6 0.9 1.2 1.5 1.8

Figure 13. Longitude-height structures of moisture advection (10^{-6} g kg^{-1} s^{-1}) calculated by zero lag-regression of 20-100 day band-pass-filtered anomalous horizontal moisture advection against Indian Ocean precipitation (80-90°E; 5°S-5°N). (a) is for observation and (b), (d), (f) are for simulations with SAS, TDK, and KFMT schemes respectively. (c), (e), (g) are the differences between 3 pairs of simulations. Regression is scaled to 3 mm d^{-1} precipitation rate. Fields are averaged between 10°S and 10°N.

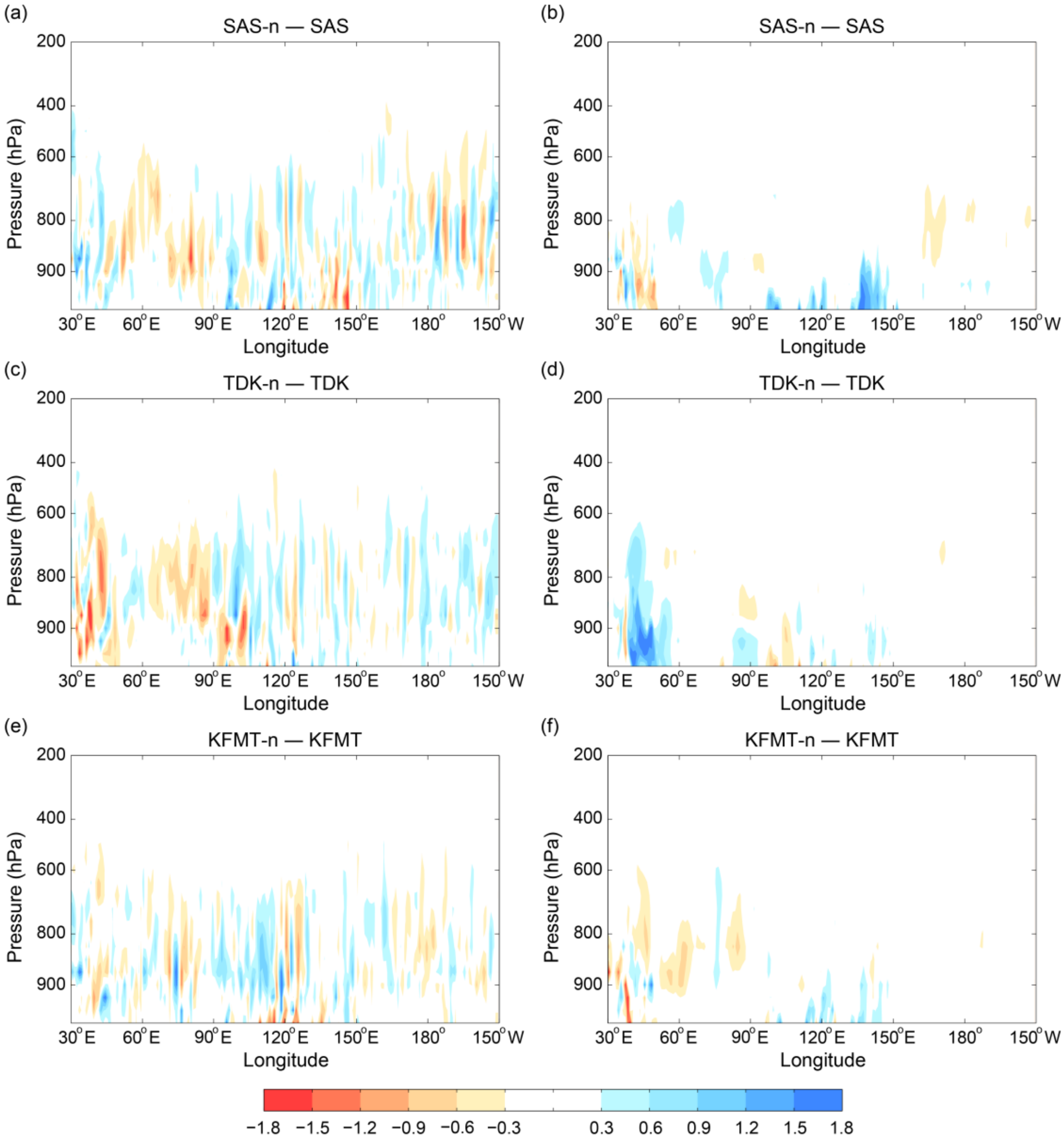

Figure 14. As in Fig. 13 (c), (e) and (g), but for the zonal (a, c, e) and meridional (b, d, f) moisture advection (10^{-6} g kg^{-1} s^{-1}).

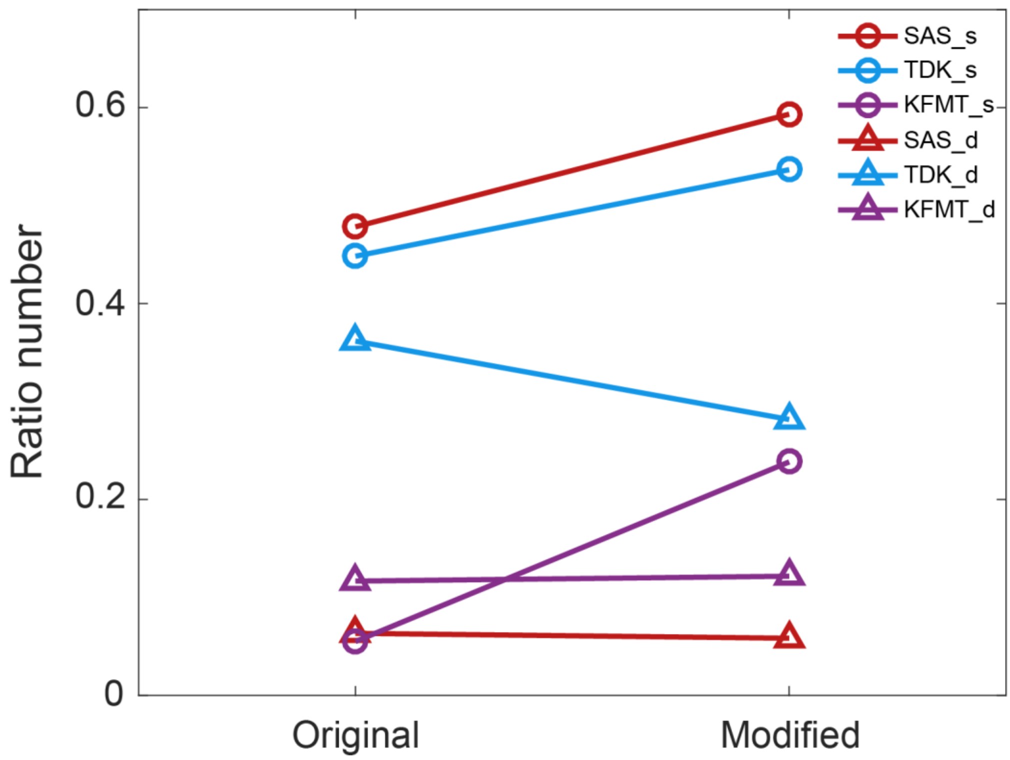

Figure 15. Ratio number (occurrence times averaged by total time steps and the number of horizontal grids in the region of 60-180°E, 15°S-15°N) change for shallow (circle) and deep (triangle) convection in 3 pairs of simulations with different CP schemes.

Non-Rendered Figure#01

Click here to access/download
Non-Rendered Figure
Fig1.pdf

Click here to access/download

Non-Rendered Figure

Fig4.pdf

Non-Rendered Figure#05

Click here to access/download
Non-Rendered Figure
Fig5.pdf

Click here to access/download
Non-Rendered Figure
Fig7.pdf

Non-Rendered Figure#08

Click here to access/download
Non-Rendered Figure
Fig8.pdf

Click here to access/download

Non-Rendered Figure

Fig9.pdf

Non-Rendered Figure#10

Click here to access/download
Non-Rendered Figure
Fig10.pdf

Non-Rendered Figure#12

Click here to access/download
Non-Rendered Figure
Fig12.pdf

Click here to access/download
Non-Rendered Figure
Fig14.pdf

Non-Rendered Figure#15

Click here to access/download
Non-Rendered Figure
Fig15.pdf